OPTICALLY ENHANCING EVENT-BASED VISION

by

Sebastian Valencia

A Thesis Submitted to the Faculty of the

James C. Wyant College of Optical Sciences

In Partial Fulfillment of the Requirements

For the Degree of

MASTER OF SCIENCE

In the Graduate College

THE UNIVERSITY OF ARIZONA

2023

THE UNIVERSITY OF ARIZONA
GRADUATE COLLEGE

As members of the Master's Committee, we certify that we have read the thesis prepared by **Sebastian Valencia**, titled ***Optically Enhancing Event-Based Vision*** and recommend that it be accepted as fulfilling the thesis requirement for the Master's Degree.

Amit Date: 4/26/23
Professor Amit Ashok

Date: 4/26/23
Professor Robert A. Norwood

Michael J. Nofziger Date: 4/26/23
Professor Michael J. Nofziger

Final approval and acceptance of this thesis is contingent upon the candidate's submission of the final copies of the thesis to the Graduate College.

I hereby certify that I have read this thesis prepared under my direction and recommend that it be accepted as fulfilling the Master's requirement.

Amit Date: 5/04/23
Professor Amit Ashok
Master's Thesis Committee Chair
Wyant College of Optical Sciences

Acknowledgements

Throughout the completion of this thesis, I have received an appreciable amount of support.

I would first like to thank my advisor, Dr. Amit Ashok, who has so generously provided guidance in all-things optics for the past two years. Thank you for giving me the freedom to mature as an optical engineer, and for all your advice and encouragement that I will cherish throughout my career.

I would also like to thank my lab colleagues and Joseph Cox, who I have worked very closely on this project with and had the opportunity to learn a great deal from.

This Thesis is based on research sponsored by Air Force Research Laboratory (AFRL) under agreement number FA9451-20-1-0005. A debt of gratitude is owed to Dr. Nicholas Morley and AFRL staff who made this work possible.

Finally, I would like to thank my parents, Horacio, and Corina, and brothers, Horacio and Marcel, for their never-ending love and support towards my studies. I could not have asked for a better family.

“Hace más el que quiere que el que puede.”

Table of Contents

List of Figures

List of Tables

Abstract

As an asynchronous imaging sensor with integrated change-detection capabilities, EBS can detect temporal changes in scene brightness as they are happening. However, its capability to detect these changes is implemented in electronics and limits the ability to detect low-contrast objects and generates significant noise, both of which hinder the ability to detect objects of interest. Optical spatial high-pass filtering, and optical photocurrent biasing is introduced to address two key Event-Based Sensor (EBS) limitations in low contrast sensitivity and low-light shot noise. The low-contrast sensitivity of EBS may be improved with optical, coherent high-pass spatial frequency filtering (HPF). This provides contrast amplification to imaged features associated with sharp edges and fine details, increasing the probability of detection of low-contrast moving objects. We present optical HPF to improve detection performance in Event-Based systems. This approach demonstrates a hardware-based solution to improving overall Event-Based system contrast sensitivity by pre-filtering imaged scenes in the optical domain. Measurements show that objects containing features with contrasts as low as 3.53% are discernable, which enables object detection with triple the sensitivity of the standalone EBS. Regarding the noise problem, the sensor's usability in low-light conditions is greatly limited by shot noise from photons and from sensor transistor circuitry. Particularly, low illumination levels signals are limited by parasitic dark current which becomes confused for objects of interest and limits overall signal-to-noise ratio (SNR). EBS noise behavior as a function of illumination level is well documented in literature and suggests that there exists an optimal background illumination level for noise minimization. This work introduces the development of passive noise correction via a synthetic injection of a spatially homogenous light field into the EBS' imaging path. This circumvents significant low-level illumination noise with up to 5x boost in normalized signal minus noise ratio, prior to post-processed noise filtering. This work may guide future development of optical improvements to the EBS and suggests improved practices for enhancing overall system performance.

Chapter 1: Introduction: Event-Based Sensor Technology

This thesis is comprised of two novel methods which address two significant performance limitations to the Event-Based Sensor (EBS): low contrast sensitivity and high noise levels in low-light conditions. Chapter 1 introduces the pertinent technical background and associated event-generation theory for Event-Based Sensors to lay the foundation for these methods.

1.1 Description & Advantages

Effective change-detection and tracking is a necessary task in applications requiring real-time information on objects of interest in an imaged scene. However, usage of traditional frame-based sensors is limited by factors including read-out bandwidth, dynamic range, latency, and temporal resolution. The Event-Based Sensor is a promising technology for performing beyond these limitations. The EBS' promise comes from its design as a change-detection camera that is sensitive to relative irradiance changes when and where they occur in an imaged scene [1], making these cameras particularly well suited for real-time motion awareness. At the focal plane, these variations in irradiance are asynchronously detected at each pixel, generating an event. Events are generated when a change in log-irradiance exceeds a specified threshold, providing the location in the imaged field, timestamp, and polarity of in-scene irradiance fluctuations. The EBS reads out measured information in Address-Event Representation (AER) format to produce a flow of information in the form of this event data structure. AER is simply a list of events, as opposed to traditional frame format which provides a well-ordered list of intensity values.

The event-logging process done at the pixel level is characterized by a change in log irradiance that exceeds a pair of temporal contrast thresholds for ON and OFF events [2]. The event rate (ON or OFF events) is dependent on temporal contrast (TC) and the temporal contrast threshold (θ) and can be approximated at each pixel as:

$$\boldsymbol{Event\ Rate(t)} \approx \frac{\boldsymbol{TC(t)}}{\boldsymbol{\theta}} = \frac{\boldsymbol{1}}{\boldsymbol{\theta}}\frac{\boldsymbol{d}}{\boldsymbol{dt}}\mathbf{ln}(\boldsymbol{I}) = \frac{\boldsymbol{\Delta L}}{\boldsymbol{\theta}} \qquad \mathbf{(1)}$$

where $\boldsymbol{I}$ is the photocurrent generated at an individual pixel. Event-Based Sensors react to fluctuations in logarithmic photocurrent (ΔL). Photocurrent is proportional to intensity (brightness) and its fluctuations may be caused by moving edges in a captured scene that generate events. Biasing circuitry within the EBS is responsible for adjusting the event temporal contrast thresholds' magnitude and the number of events that will be produced as a result. These adjustments are controlled by the ratio between bias currents in the differencing amplifier and comparators. The EBS detects both increases and decreases in irradiance, whose polarity is denoted by ON and OFF events. This EBS behavior may also be approximated by a subtract-and-threshold function in which the previous ($E_{Previous}$) and current ($E_{Current}$) irradiance states measured by an individual pixel are differenced [3]. In this model, an event is generated when the ratio change in irradiance difference surpasses a threshold, known as the temporal contrast (TC) of the EBS:

$$\frac{E_{Current} - E_{Previous}}{E_{Previous}} = \frac{E_{Current}}{E_{Previous}} - 1 > TC \quad (2)$$

Although the EBS works on log irradiance as opposed to irradiance, event generation may be approximated as a percent-change difference operation when operating near low-contrast scene irradiances and is expected to best mimic actual EBS behavior in scenes where the ratios of irradiance and log irradiance ratio ($\frac{E_{Current}}{E_{Previous}}$) are sufficiently close to one.

Like with other sensors and imagers, extracting high-dimensional information from data sequences to take decisive actions is an important class of EBS applications. Examples of such implementations include object/gesture recognition [4], traffic monitoring with vehicle speed estimation [5], and object tracking [6]. EBS technology has potential for outperformance of the frame-based counterpart in these applications through several unique traits. These traits include reduced motion blur, scene information compression, and dynamic range [7] [8] [9]. These traits are derived from the EBS's asynchronous data collection, contrasting with frame-based imagers' synchronous frame capture process. When considering object detection and tracking scenarios, conventional frame-based imagers may under sample the motion of an object in between frames while simultaneously oversampling an unchanged background. For example, when fixed in a static position, an EBS camera triggers the pixels associated with the movement of an object stimulus and is insensitive to the stationary background. This elimination of the redundancy of oversampled scene elements such as the background enables more efficient usage of the sensor resources. This efficiency contrasts with frame-based cameras, which can employ post-imaging methods that subtract consecutive, fully-sampled frames to find discrepancies indicating the presence of an object of interest. As EBS only records local irradiance changes, there is an overall reduction in bandwidth and an effective increase in spatio-temporal resolution [10].

Event-Based Sensors are well-suited for high-speed measurements due to the increased spatio-temporal resolution. Current EBS cameras, such as those sold by iniVation, carry temporal resolution in the hundred microsecond range [11], with typical latencies of less than a millisecond [12]. These measurements may be used in many ways, for example simultaneous event capture from the EBS may be combined with the data collection of low-speed frame-based imagers to enable high-speed frame-based video reconstruction [13] [14].

Event-Based Sensor (EBS) imagers are attractive for their high dynamic range (HDR) enabled from their ability to detect logarithmic changes in light intensity over a wide illumination level range. Conventional frame-based imagers typically have a dynamic range of up to 60 dB [7] whereas the EBS may have up to 120 dB of dynamic range [12] since logged events are always relative (log) irradiance changes. However, this logarithmic compression reduces EBS's contrast sensitivity due to imprecise analog electronic operations operating on the compressed signal [15]. In this work, we focus on mitigating this contrast limitation through exploring a hardware solution in the optical domain, presenting an optical field better suited for EBS's high contrast requirements. While this approach was originally explored for object detection and tracking applications, we expect that it will find use in other fields such as microscopy and biological imaging.

1.2 Working Principles & Circuitry

EBS' ability to detect changes in scene brightness is enabled by its analog circuitry described in detail in existing literature [1] [2]. Pixels in Event-Based Sensors register sequences of log intensity fluctuations above some predefined magnitudes. This function is modeled after the way fluctuations are perceived by the human visual system [16]. Pixels store log intensity values after an event is triggered and await a log intensity change with respect to these stored values, encoded as $e(p, x, y, t)$ using the AER protocol. Figure 1 illustrates the EBS pixel's asynchronous operation for detecting changes.

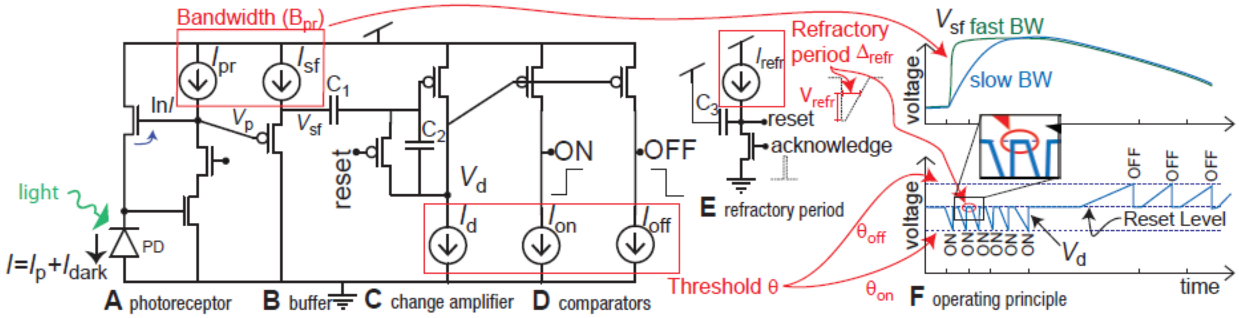

Figure 1. EBS analog circuitry with components labelled and principle of operation, from [17].

Photocurrent I is translated into a voltage V_p that logarithmically scales with the photocurrent, where irradiance is directly proportional to photocurrent. Therefore, event output may be represented when the following is true:

$$\ln\left(\frac{E_{Current}}{E_{Previous}}\right) > TC \rightarrow \frac{E_{Current}}{E_{Previous}} > e^{TC} \quad \textbf{(3)}$$

EBS pixels will produce photocurrent I, which is composed of signal photocurrent Ip as well as sensor dark photocurrent I_{Dark}. Rapid spikes in the converted voltage are attenuated by a source follower (SF) buffer and fed into a switched capacitor change amplifier which magnifies log intensity changes from the stored value of a previously triggered event to send out V_{diff}. A pixel then uses two voltage comparators to compare V_{diff} to ON and OFF thresholds and generate a positive or negative polarity event accordingly. The ratio between bias currents $\mathrm{I_{OFF}}$, I_{ON}, and I_D are responsible for setting event thresholds. A rest pulse is sent out to hold V_{diff} for a configured refractory period t_{refr} that is controlled by I_{refr} , during which the pixel does not respond to stimuli change. The sensors' ability to respond fast (temporal bandwidth) is dictated by the readout circuity biases I_{pr} and I_{sf}, and input illumination levels. These five bias currents ultimately characterize sensor performance. AER event streams produced by the EBS are readily processable, for fine information extraction of a host of task-specific applications.

1.3 Event-Generation Theory

To model EBS event generation, Equation 1 presents the event rate as the ratio of the log photocurrent and the contrast threshold. Under conditions of constant source-to-background illumination and constant velocity, the log photocurrent approximates to:

$$\Delta \boldsymbol{L} \approx -\boldsymbol{\nabla L} \cdot \boldsymbol{v} \cdot \Delta \boldsymbol{t} \qquad \textbf{(4)}$$

The above approximation is valid for small, fixed time increments ($\Delta \boldsymbol{t}$) [18]. Therefore, temporal contrast may be approximated as a function of brightness gradient $\boldsymbol{\nabla L}$ (spatial contrast corresponding to an $Ln(E)$ change in e-folds) and velocity (pixels / second). When an object contains horizontal brightness gradients, ∇L becomes:

$$\boldsymbol{\nabla L} = \begin{bmatrix} \boldsymbol{\partial_x L} \\ \boldsymbol{\partial_y L} \end{bmatrix} = \begin{bmatrix} \boldsymbol{\partial_x L} \\ \boldsymbol{0} \end{bmatrix} \qquad \textbf{(5)}$$

By relating Equations 1, 4, and 5, a direct relation between the event rate and spatial contrast may then be established. Considering separate contributions for ON and OFF events (with separate temporal contrast thresholds) results in the following approximate event rates:

$$\boldsymbol{ER_{OFF}} \approx |\boldsymbol{\partial_x}(\boldsymbol{L})|\boldsymbol{v}\Delta\boldsymbol{t} \left(\frac{\boldsymbol{1}}{|\boldsymbol{\theta_{OFF}}|}\right) \qquad \textbf{(6)}$$

$$\boldsymbol{ER_{ON}} \approx |\boldsymbol{\partial_x}(\boldsymbol{L})|\boldsymbol{v}\Delta\boldsymbol{t} \left(\frac{\boldsymbol{1}}{|\boldsymbol{\theta_{ON}}|}\right) \qquad \textbf{(7)}$$

Although event generation occurs on relative irradiance changes, event output quality is best when background irradiance levels are low such that signal-to-background ratio is highest. An increase in background irradiance levels will reduce the magnitude of $\boldsymbol{\nabla L}$ compared to a signal without any background level irradiance. A modified version of Equation 2 demonstrates how under some constant background irradiance ($\boldsymbol{B}$), temporal contrast will be reduced and thus less likely to trigger events.

$$\frac{(\boldsymbol{E_{Current}}+\boldsymbol{B})-(\boldsymbol{E_{Previous}}+\boldsymbol{B})}{\boldsymbol{E_{Previous}}+\boldsymbol{B}}=\frac{\boldsymbol{E_{Current}}+\boldsymbol{B}}{\boldsymbol{E_{Previous}}+\boldsymbol{B}}-\mathbf{1}>\boldsymbol{TC} \qquad \textbf{(8)}$$

From Equation 8, it becomes apparent that event generation for edges and brightness gradients will be maximized when $\boldsymbol{B} \cong 0$. However, object edges and brightness transitions tend to not be spatially abrupt changes. The individual temporal contrasts perceived by each pixel that is within the span of an edge depends on the speed of induced motion and integration time (t_{int}) of the EBS. For a given integration cycle, the temporal contrast perceived by EBS pixels is given by:

$$\frac{\boldsymbol{I_i}(\boldsymbol{x_3}+\boldsymbol{v}\cdot\boldsymbol{t_{int}},\boldsymbol{y_3})-\boldsymbol{I_i}(\boldsymbol{x_3},\boldsymbol{y_3})}{\boldsymbol{I_i}(\boldsymbol{x_3},\boldsymbol{y_3})}>\boldsymbol{TC} \qquad \textbf{(9)}$$

Using Equations 6-9, the total event rate from all activated pixels after filtering may be predicted.

Chapter 2: Improving Contrast Sensitivity

With its integrated change-detection circuit, the EBS benefits from improvements in its ability to register low-contrast edges between an object of interest and other features in the scene. This chapter discusses this limitation and details our approach to resolve it when imaging coherently illuminated scenes.

2.1 Contrast Sensitivity Limitation

When contrast in real-world scene elements is non-ideal, such as when a moving object may blend in with the background (i.e., overcast clouds and other atmospheric disturbances), the EBS contrast sensitivity is limiting. Here, low contrast leads to reductions in information-bearing events about moving objects. Simply put, the EBS temporal contrast sensitivity is too low in many applications. The minimum reported contrast sensitivity ranges from 9% to 14% across the range of available EBS cameras [12] [18], although measured values may show these to be higher [19]. Contrast sensitivity of EBS cameras is controlled by bias currents set at each pixel but defined as a sensor-wide constant value. These currents drive threshold and set voltages in the comparators that detect increases or decreases in light intensity exceeding threshold values [2]. Event temporal contrast thresholds may be lowered (within sensor model's limits) through software (e.g., jAER or DV [20] [21]) by adjusting bias current parameters that are responsible for setting the TC. Increasing low-contrast visibility through the EBS may be achieved by skewing bias current ratios to trigger off lower irradiance fluctuations. However, setting minimum allowable contrast sensitivity may result in increasing false detection probabilities (i.e., noise) and limited by overall voltage gain and capacitive ratio [22]. This notion highlights how the overall EBS effectiveness for successful object detection is reduced when the effective event signal-to-noise ratio (SNR) is decreased [23], and underscores the importance of addressing EBS contrast sensitivity.

2.2 Current Approaches

Several attempts to improve contrast sensitivity for EBS have been made by modifying the change-detection electronics, achieving temporal contrasts as low as 1% [22] [24] [25]. Limitations to low contrast include EBS noise (i.e., shot noise from photons and comparator circuitry) shrouding intensity differences in the detected signal, and transistor mismatches further creating complications in setting low thresholds [26]. At low temporal contrasts, the EBS is limited by shot noise where individual pixels react to noise fluctuations in photocurrent. Such fluctuations regularly surpass contrast thresholds and create noisy, high event-rate data streams [18]. This may lead to readout saturation, dropped events, and latencies that prevent real-time output performance [17]. Algorithmic adjustments to bias current parameters (via jAER) for active threshold control have also been reported. Such algorithms utilize optimized biases and globally alter the sampling rate of pixels as a function of the measured event rate for dark and bright illumination conditions [27] [28].

2.3 Proposed Method

In this work, we aim to improve the resolvability of low-contrast objects and features of interest by improving the overall EBS imaging system's contrast response through optical domain control. As such, our approach does not require any modifications to EBS circuitry, or supplemental algorithms for automatic control of temporal contrast thresholds. The proposed method involves pre-processing the coherently imaged scene using a spatial high-pass filter for better detection and resolution of low-contrast objects of interest.

Spatial frequency filters are common in coherent, optical image processing for modulation of specific spatial frequencies that combine an image, which is defined as a two-dimensional pixel-intensity function [29]. A high-pass filter attenuates all spatial frequencies below some cutoff frequency. To enhance edges and fine details, high-pass spatial frequency filters are used to produce sharpened images [30]. When an image is altered to retain high frequencies, smooth features are removed, and sharp details dominate. As EBS is highly responsive to object edges and other sharp details, applying the optical high-pass filter here passes these details, while removing the smooth features, amplifying the contrast without degrading the event stream's information content. In other words, an application already tailored to EBS's change-detection capabilities achieves contrast benefits without significant information loss, because the change-detection acts as a second high-pass filter. These filtering operations are done in the frequency domain of an image signal through Fourier optics.

Under the conditions of coherent illumination, a converging lens (positive focal length) can perform two-dimensional Fourier Transformations. Coherent waves exhibit a definite phase relationship, allowing their interference patterns to be predicted. A coherent optical system can then use this transform and its inverse to apply a spatial filter to the incident light field. As such, this technique requires active object illumination to create a coherent optical field. To physically achieve contrast amplification, an Optical High-Pass Filter (HPF) is employed, in which a small circular obstruction is centralized at the Fourier Plane. Low spatial frequencies are responsible for forming the overall layout of an image, while higher spatial frequencies establish the edges of scene elements and finer details. HPF obstructs lower spatial frequencies located at or near the middle of the imaged object's diffraction pattern in the Fourier Plane as seen with an example image in Figure 2. As the EBS responds to per-pixel irradiance changes from moving features, HPF will generally allow for capturing only the changing information with higher SNR.

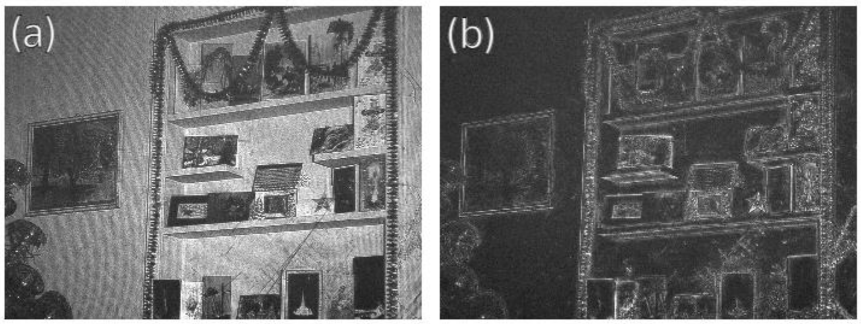

Figure 2. Example of (a) Standard and (b) High-Pass Filtered Images of a shelf with various objects (under coherent illumination).

This method explores the potential of EBS technology to improve as an effective detector and tracker due to increased contrast and event generation for low contrast moving objects. With a means of providing contrast boosts, the EBS may register previously imperceptible low-contrast features.

2.4 Optical High-Pass Spatial Filtering (HPF)

The optical spatial filtering system employed in this work is a 4f system as shown in Figure 3. Monochromatic light originates from a point source (S) and is collimated by a lens (L_C) to create a coherent illumination object field $u_o(x_1, y_1)$ of a transparency object at the input plane (P_{Input}). The first Fourier lens in the 4f system (L_1) transforms the input into the spatial frequency domain.

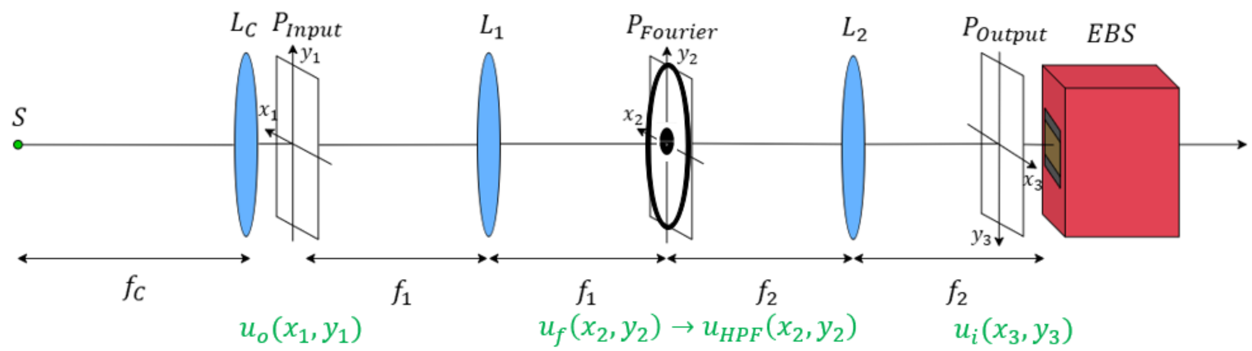

Figure 3. 4f spatial filtering imaging system where S is monochromatic illumination source; $f_c$is the focal length of collimation lens L_c; $f_1$is the focal length of first Fourier lens L_1; $f_2$is the focal length of second Fourier lens L_2; P_{Input}, object plane; $P_{Fourier}$, Fourier plane; P_{Output} , Image plane.

When the object plane is located a focal length away from a converging lens, an exact Fourier transform relationship between the incident and focal plane field is expressed [29]:

$$\boldsymbol{u_f(x_2, y_2) = C_1 \cdot U_o\left(\frac{x_2}{\lambda f_1}, \frac{y_2}{\lambda f_1}\right)} \qquad \textbf{(10)}$$

where $U_o(f_{x_1}, f_{y_1}) = \mathcal{F}_2(u_o(x_1, y_1))$ and $u_f(x_2, y_2)$ is the Fourier Transform of the input field at the Fourier Plane ($P_{Fourier}$).The spatial frequencies f_x and f_y at $P_{Fourier}$ are related to spatial coordinates (x_2, y_2) and illumination wavelength (λ) through $f_x = \frac{x_2}{\lambda f_1}$, and $f_y = \frac{y_2}{\lambda f_1}$. A circular HPF mask is located here to suppress low-frequency information, allowing light to pass through according to the aperture function $p_{Fourier}(x_2, y_2) = cyl\left(\frac{r}{W_2}\right) - cyl\left(\frac{r}{W_1}\right)$ in the spatial domain, where $r = \sqrt{(x_2)^2 + (y_2)^2}$, and W_1 and W_2 are the diameters of the HPF mask, and the clear aperture respectively. The filtered field is the product of object FT and pupil function at $P_{Fourier}$, which details spatial frequency throughput:

$$\boldsymbol{u_{HPF}(x_2, y_2) = u_f(x_2, y_2) \cdot p_{Fourier}(x_2, y_2)} \qquad \textbf{(11)}$$

The reconstruction of the altered frequency spectrum into the spatial domain is handled by the second Fourier lens in the 4F system (L_2) and located a focal length away from the lens. The final output at P_{Output} is where the EBS is positioned such that a focused image is projected onto the bare camera sensor. The resultant output function can be written as:

$$\boldsymbol{u_i(x_3, y_3) = C_2 \cdot U_{HPF}\left(\frac{x_3}{\lambda f_2}, \frac{y_3}{\lambda f_2}\right)}$$

$$\boldsymbol{= C_2 \cdot C_1 \cdot u_o\left(-\frac{f_2}{f_1}x_3, -\frac{f_2}{f_1}y_3\right) * P_{Fourier}\left(\frac{x_3}{\lambda f_2}, \frac{y_3}{\lambda f_2}\right)} \qquad \textbf{(12)}$$

where $U_{HPF}\left(f_{x_2}, f_{y_2}\right) = \mathcal{F}_2\left(u_{HPF}(x_2, y_2)\right)$. The ratio between the focal lengths for the two Fourier Lenses, $f_2 \,/\, f_1$, is the overall system magnification for the imaged object. The final output coordinate system at P_{Output} is inverted to simplify convention as two FT operations were used sequentially.

$$\boldsymbol{I_i(x_3, y_3) = |u_i(x_3, y_3)|^2} \qquad \textbf{(13)}$$

The irradiance at the EBS $I_i(x_3, y_3)$, is related to the output image field as seen in Equation 13 above.

2.5 Experiment Design & Analysis

Here, we discuss the components forming our HPF setup and its expected results based on the framework established in Section 2.4.

A transmissive 4f HPF system is constructed to image a transparent object and evaluate overall EBS performance. To measure the lowest possible contrast the EBS can detect with this HPF method, a transparent object with regions of different transmission levels was required. For this experiment, a custom fabrication, which consisted of a clear substrate (Figure 4) with a photoresist spin coating, was procured. The slide contains five different regions which attenuate transmitted light according to the photoresist thickness and thus effectively acts as a stepped neutral density filter. A coherent illumination source at 543 nm wavelength is employed in the experiment. An optical power sensor calibrated at this wavelength was used to measure irradiance transmittance of each region and compute successive boundary contrasts.

Figure 4. Photoresist coated slide having low contrasts with regions 1 to 5 (from right to left).

As previously mentioned, all event-based technology is susceptible to generation of undesired events due to intrinsic noise from circuitry and shot noise from photons. These noise sources are known to affect event rates significantly, with a dependency on absolute illumination levels [2] [31]. These noise-induced event rates must be properly accounted for establishing accurate event rate predictions in both non-HPF and HPF cases. Thus, an assessment of this event rate production per illumination levels was conducted. Noise event rate measurements are shown in Figure 5.

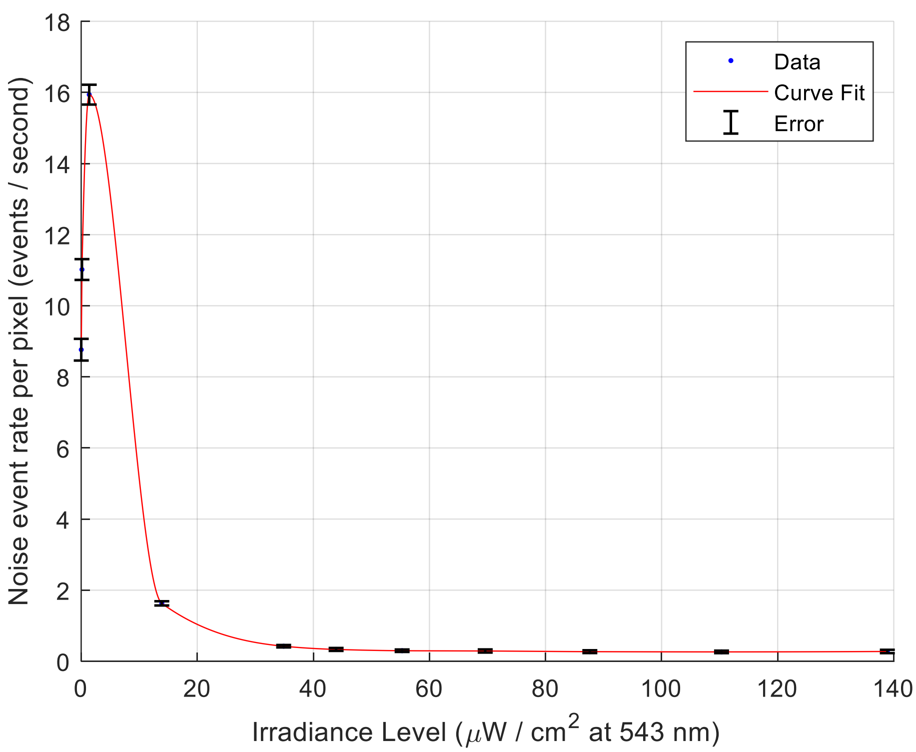

Figure 5. Noise-induced event rate as a function of ambient irradiance levels measured at EBS.

Our noise measurement setup employed a uniform background with known, ambient illumination level which is imaged by the EBS. Neutral density filters were positioned directly in front of the EBS camera lens such that irradiance at the sensor plane is attenuated to various levels. Per-pixel event-rate for each irradiance was measured using EBS jAER's interface. The measurements in Figure 5 depict how low scene illumination yields a higher, detector-noise dominated event rate, whereas higher scene illumination results in fewer triggered events that are shot-noise dominated. Event rates expected from the five regions of the transparent object without the HPF enabled are quantified from the noise event rate's curve fit. The results are seen in Table 1 below.

Table 1. Measured contrast percentages (relative to successive region) and predicted event rates for transparency slide regions.

Region	Average Irradiance (mW/m^2)	Percent Contrast relative to next region	Expected Per-Pixel Event-Rate from Illumination Level (Events / Second)
1	358.9	8.17 ± 0.09	0.41 ± 0.03
2	329.6	6.69 ± 0.08	0.46 ± 0.03
3	307.5	5.41 ± 0.05	0.51 ± 0.04
4	290.9	3.53 ± 0.04	0.56 ± 0.04
5	280.6	NA	0.59 ± 0.04

The photoresist is deposited with a 5 μm resolution transition between each region. Using a 4f system magnification of 0.5, the fine edges between regions on the slide are predicted to be as large as 2.5 μm at the rear focal plane where the EBS is located. The predicted geometrical width of transitions is much smaller than the 18.5 μm pixel pitch of the DAVIS346 Camera used. A visible boundary will generate events corresponding to the contrast between the first region of interest and the second region of interest. Having the width of boundary transitions be much smaller than an EBS pixel greatly reduces the risk of having misleading event generation from an intermediate region between the two uniform regions.

A 309 μm diameter central obstruction was implemented as the High Pass Filter mask at the Fourier Plane. The circular beam block is mounted onto a standard lens mount as shown in Figure 6. The strength of the filtering effect depends on the size of the obstruction. The mask used in this experiment was one that was readily available for HPF proof-of-concept and was not tailored for maximum HPF effect.

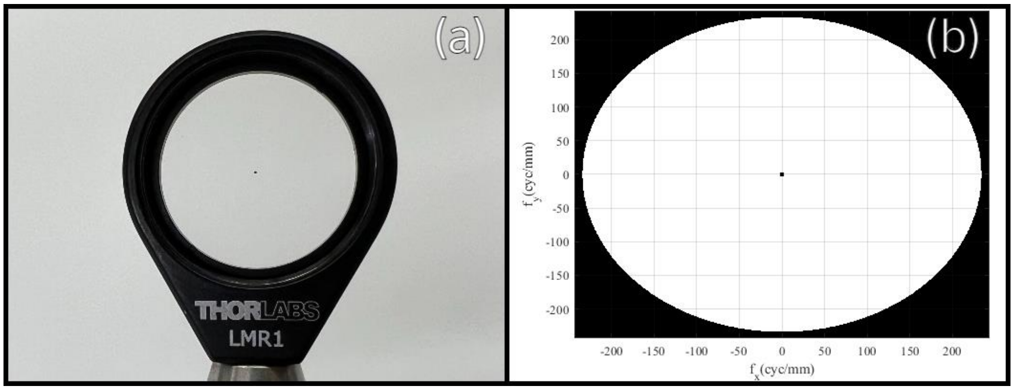

Figure 6. 0.309 mm diameter HPF mask (a) and corresponding representation in spatial frequency Domain (b).

To simulate motion and generate events, the EBS was mounted on a motorized stage that provided linear horizontal motion at a constant speed. The EBS output events are binned to fixed 20 millisecond time slices (Δt), while the moving boundary edge is set to a constant velocity (towards decreasing slide transmission) of 2 millimeters per second. This velocity corresponds to 109 pixels per second (v) at the sensor plane. For this given stimulus velocity and integration time, a single EBS pixel will respond to the contrast defined between two points in the stimulus signal with spatial separation of $v\Delta t = d_\rho \approx 2$ pixels. EBS contrast sensitivity was set at the nominal event thresholds of 21.2% (0.193 e-folds) and -18.1% (-0.200 e-folds) for ON and OFF events respectively via the jAER User-Friendly control panel. The overall 4f HPF transmissive system is seen in Figure 7 with each subsystem labelled. Collection methods are discussed further along with results in Chapter 4.1.

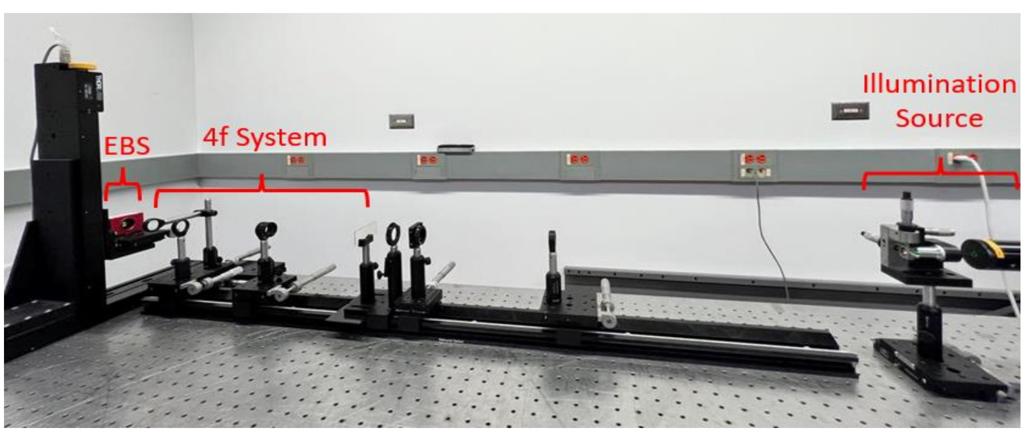

Figure 7. Overall transmissive HPF system layout

Based on the system model described in Equations 6-9, we obtain a theoretical estimate of irradiance and event rates before and after HPF, shown in Figure 8.

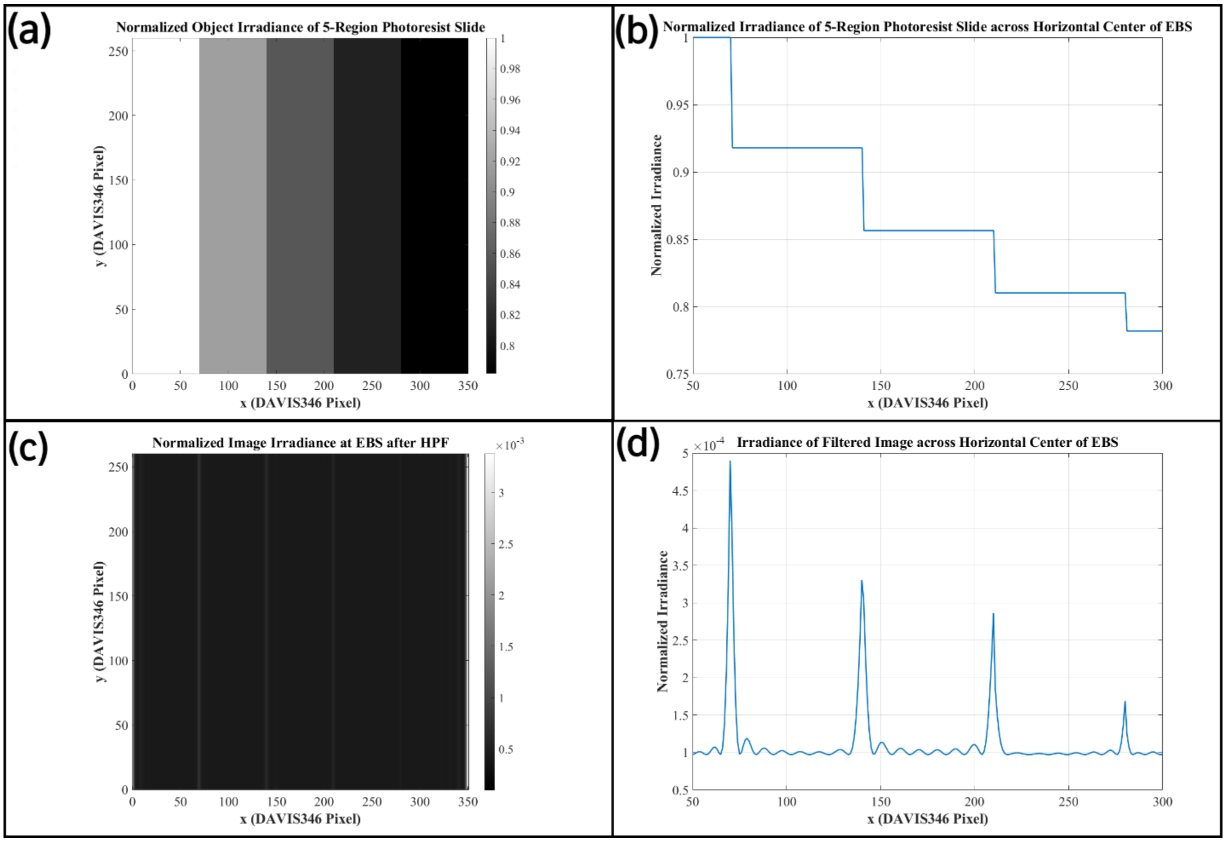

Figure 8. Top Row: Simulated object of photoresist-coated slide (a); Irradiance profile of object before filtering across EBS sensor (b). Bottom Row: Simulated image of object after propagating through HPF system as perceived by EBS (c); Irradiance profile after HPF across EBS sensor (d). All irradiances are normalized to max irradiance prior to filtering (region 1).

As seen in the above figure, High-Pass Filtering works to greatly boost the relative contrast of edges corresponding to brightness transitions. Furthermore, the width of the four boundaries in Figure 8(b) now span 10 pixels after spatial filtering as seen in Figure 8(d). As discussed in Section 2.3, the increased boundary width produces several contrast transitions across the 10 pixels which will intensify event generation. Given $d_\rho \approx 2$ pixels, the percent contrast perceived by each pixel as the boundary moves across the imaged view are plotted in Figure 9 and are referenced with respect to largest irradiance (peak) of each HPF-enhanced edge of Figure 8(d). These contrasts are used to compute the sum event rate generated for each enhanced boundary using Equations 6-7.

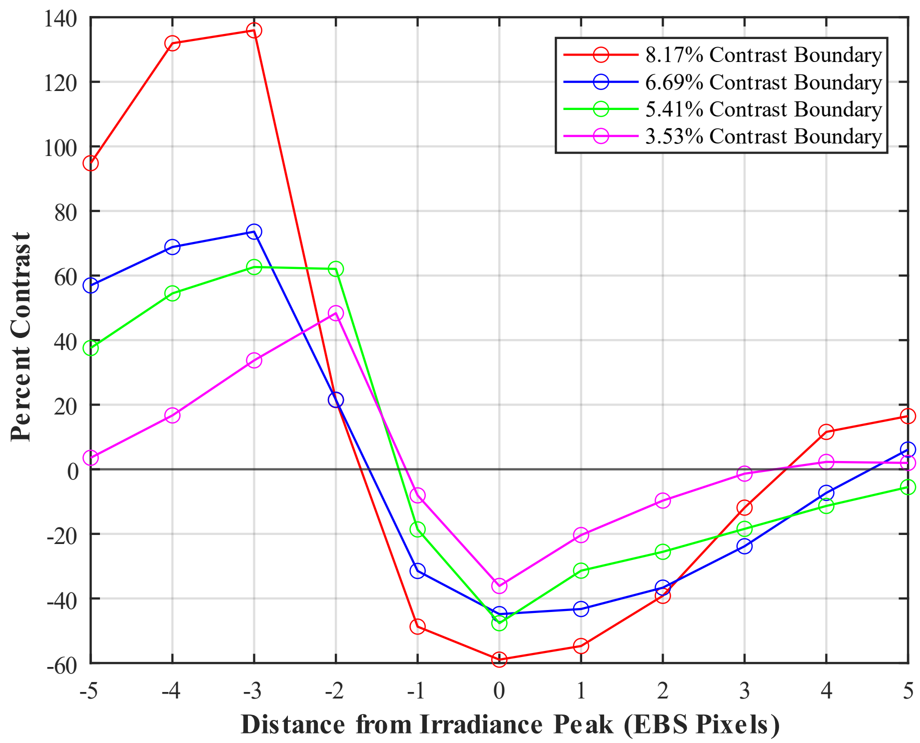

Figure 9. Predicted contrast percentages perceived by each pixel for d_ρ = 2 over span of HPF-enhanced boundaries.

Expected event rates for each boundary prior to and after HPF are tabulated in Table 2. The simulated event rate before and after amplification is computed, and the figure of merit, Contrast Amplification Factor, quantifies the effect of the HPF. These simulated results set expectations for experimental HPF implementation.

Table 2. Predicted event rates at low-contrast boundaries (per 20 millisecond bin).

	Boundary			
	1st	**2nd**	**3rd**	**4th**
Non-HPF				
Initial Transition Average Contrast [%]	8.17	6.69	5.41	3.53
Total Per-Pixel Event Rate with Noise Accounted [ON + OFF Events / sec]	2.15 ± 0.05	1.90 ± 0.05	1.68 ± 0.04	1.33 ± 0.04
HPF				
Total Per-Pixel Event Rate with Background Illumination Accounted [ON + OFF Events / sec]	34.72 ± 1.21	24.74 ± 0.98	17.81 ± 0.86	7.30 ± 0.45
HPF/Non-HPF Event Gain Factor				
Contrast Amplification Factor	16.1 ± 0.7	13.0 ± 0.6	10.6 ± 0.4	5.5 ± 0.4

Chapter 3: Bypassing Low-Light Noise

This chapter describes the sensor noise degradation when in low-light scenarios and probes the potential of a fully hardware-based method for denoising.

3.1 Intensity-Dependent Noise

Low-illumination level imaging holds a basis in many real-world applications for the EBS such as night-time surveillance and autonomous driving [32], wildlife observation [33], microscopy [34] [35], astronomical imaging [36], etc. However, at these low levels, EBS CMOS sensors are inherently limited by shot noise from photons and from sensor transistor circuitry noise. Particularly, at excessively low illumination levels, signals are dominated by parasitic dark current producing shot noise events and shrouding the true signal. The primary source of noise in low light environments is shown to come from reset and readout transistors whereas high illumination noise mainly originates from the photodiode. These shot noise events are the result of the unrelated arrival photons and electrons that generate random spikes in V_p, As a result, this greatly limits temporal contrast sensitivity and overall signal-to-noise ratio (SNR) [37] [38]. Furthermore, very high EBS event rates may raise the issues of readout bus saturation, bandwidth limitations, and others, leading to an overall reduction in the number of true brightness change events.

EBS noise behavior as a function of illumination level is well-documented in literature and suggests that there exists an optimal background illumination level for noise minimization and background event rates [17] [39]. The per pixel event rate for a DAVIS346 camera is measured as a function of scene spectral irradiance levels at 633 nm using an optical power meter and seen in Figure 10 below. A white posterboard is uniformly illuminated by multiple fluorescent lights imaged and imaged by the static camera. Total on-sensor irradiance is not measured but will be proportional to measured spectral irradiances at the input of camera lens and any given wavelength. Neutral density filters are placed in front of the camera lens in small steps in optical density (ΔOD = 0.1) to finely sample the event rates at numerous irradiance levels.

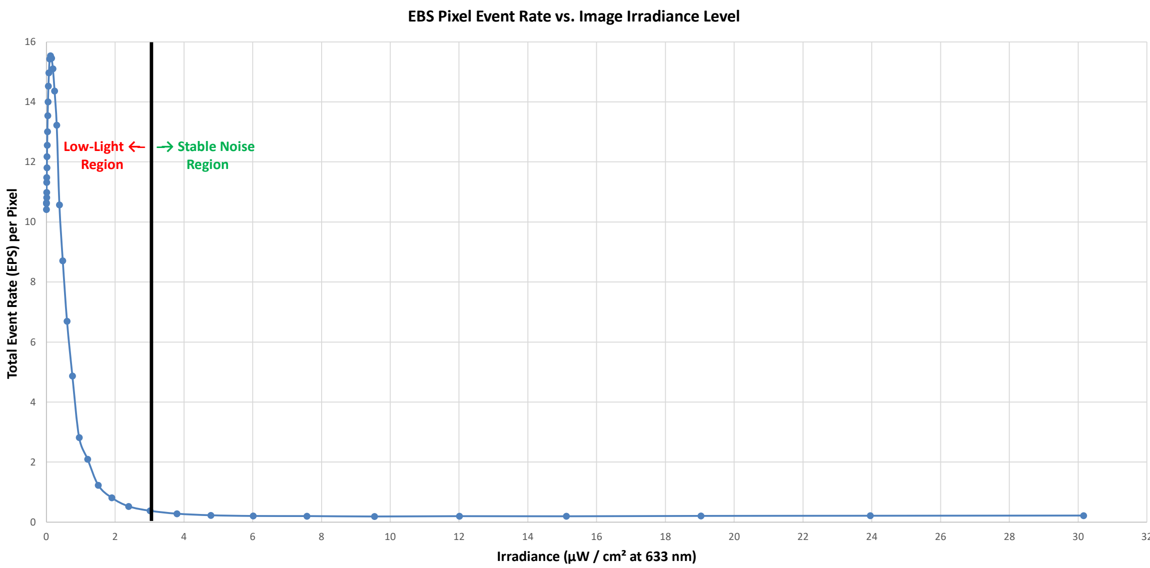

Figure 10. Pixel event rates for varying irradiances measured using power meter calibrated at 633 nm (for DAVIS346) with nominal bias parameters seen in Table 4.

The measured results in Figure 10 portray the sharp rise in noise background event rates after traversing into the low-light region, which is arbitrarily modelled to the left of the black vertical bar. Within this region, sensor noise event rates are extremely high and peak at around 15.5 events per second at 0.12 uW/cm^2 irradiance, at 633 nm. Conversely, event rates diminish and stabilize to ~ 0.2 Hz in the irradiance range to the right of the black bar. Usability in these low-light conditions has been greatly limited by noise, thus fully quantifying the sensor's performance and associated tradeoffs in this regime has yet to be completely characterized. Understanding non-ideal performance behaviors is of significant value as the EBS continues moving towards diverse applications in irregular operating environments.

3.2 Denoising Approaches

Under dim lighting, noise event rates are commonly managed with the adjustment of contrast sensitivity or photoreceptor bandwidth parameters. There has been a recent push in literature regarding the trade-offs affecting shot noise event rates through bias control, manipulating the key sensor parameters of contrast thresholds, refractory period, and bandwidths [16] Namely, in dark environments a low I_{pr} and I_{sf} may decrease background activity and bandwidth [17]. Purposefully unbalancing thresholds has been shown to reduce event rates by 80% by reducing the likelihood of successive noise events from triggering [40] [41]. However, desired signals corresponding to physical objects may be overlooked when the selected biases do not log very quickly or very small irradiance fluctuations. In some cases, higher noise rates may be largely post-processed and filtered away at the expense of elevated latency, power consumption, and data volume. Given that there is currently no coalesced standard for evaluating the quality of event streams, directly comparing these separate methods is not pragmatic.

Intelligently denoising EBS output feeds via processing has been explored extensively in numerous works in literature. The most common approaches utilize post-imaging background activity filters (BAF) to remove events without temporal correlation to other pixels in their spatial vicinity. Such filters are known as spatiotemporal correlation filters and are commonly used in jAER and other EBS software [42] [43]. These filters will pass through events that are adjacent to a processed event, which have time stamps closer than some finite time dT. Memory complications may present implementation challenges under very high event rates in the low-light region. Studies have identified inadequate performances in high-concentration scenes when memory is prematurely overridden [26]. Furthermore, a faster noise event stream increases the probability of signal events being filtered away when a spatiotemporal correlation occurs with a noise event. Although these filters may be effective at removing clutter with acceptable memory complexity in some cases, this does not alleviate the sensor readout circuity from noise at all.

Other approaches to denoising have been made through hardware neural networks and algorithms implemented with Field-Programmable Gate Arrays (FPGA) and other integrated circuits [44] [45]. These methods drop events when objects pass between the adjacent binned areas used for this type of filtering and may experience delayed processing speeds. The various hardware denoisers are also subject to tradeoffs between memory minimization and denoising accuracies which may hinder real-time performance or falsely remove desired events [46]. Other attempts have also been made to limit noise by expanding pixel size and increasing total photon collection area such that more light is accumulated [47] at the expense of sensor spatial resolution, which is already limited by the spatial extent of the EBS pixel circuit. Commercial EBS chips currently support standard silicon wavelengths up to 1.1 um [48], but the development of EBS cameras well into the infrared domain is in the works [49] [50]. Noise compensation with low-background light levels carries greater weight into the IR bands, which tend to deal in low illumination scenarios. IR EBS cameras currently in the works appear to have an additional hardware data processing layer [51], similar to the background activity filter in visible sensors [44] [45].

3.3 Optical Biasing

This work introduces the development of EBS noise correction with the synthetic injection of a spatially homogenous light field onto the EBS' imaging path to circumvent significant low-level illumination noise. We will refer to this method as optical biasing which, equivalently, consists of the addition of a padding photocurrent I_B (through irradiance padding B), such that the logged photocurrent seen in Figure 1 is equal to $I_P + I_{Dark} + I_B$. The addition of B results in a reformed version of Equation 8 for describing event generation:

$$\ln\left(\frac{E_{Current}+B}{E_{Previous}+B}\right) > TC \rightarrow \frac{E_{Current}+B}{E_{Previous}+B} > e^{TC} \quad (14)$$

A much more candid approach would be to directly administer a padding current into the pixel photodiode, which has yet to be done. Thus, the photocurrent in this work is added into the photodiode optically. This method is passive and does not rely on modifying sensor electronics, filters, or the use of active algorithms for controlling key sensor parameters (contrast thresholds, refractory period, photoreceptor bias currents, etc.) as is the case with current approaches described in Section 3.2.

This method is specifically proposed for task applications involving excessively low illumination levels, in which current noise mitigation approaches may be rivaled. Optical biasing aims to reduce significant sensor noise by shifting up imaged irradiance levels away from the low-light region and into a region with lower noise rates as seen in Figure 10. The noise reduction comes at the expense of object contrast, which, as seen in the other methods, also results in less signal event rates. However, the scale at which these two happen is not the same as the effect is greater for noise reduction. Thus, there is an opportunity for maximizing SNR by accepting some tradeoff between the two parameters. However, purely maximizing SNR is not the only thing to consider, as this may be accomplished via high contrast thresholds and lowered bandwidths such that there is minimal noise with slight levels of information-bearing signal. Considering only optical supplementation is used, a reduction in overall data volume is achieved with no computational cost and enables for improved object extraction. As discussed in the previous chapters, sensor performance is largely dependent on user-defined biases and illumination levels. Resultantly, optimal object and padding level pairs are only valid at specific illumination levels. This work only intends to showcase the value of optical biasing and present another configurable degree of freedom in the search of task-specific optimal EBS performance.

3.4 Experiment Design & Analysis

Covered in this section are the design details of the optical biasing implementation, which are used to generate predictions for expected results.

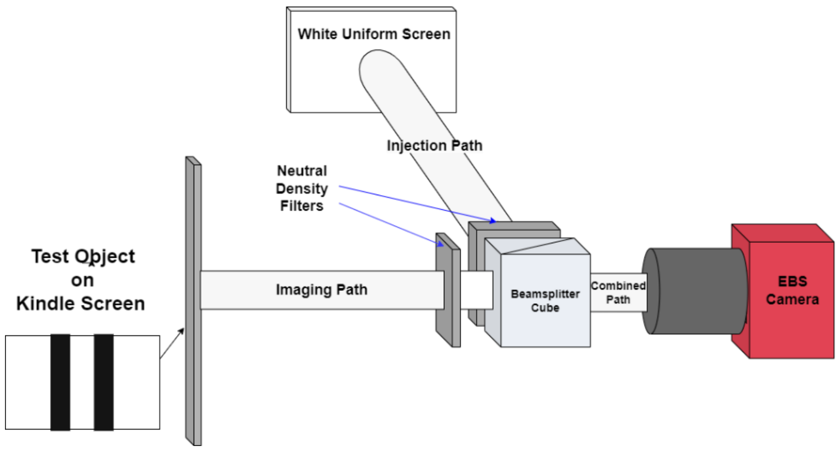

Figure 11. Optical setup with 50/50 BS cube

A 50/50 optical beamsplitter cube (BS) is placed directly in the FOV of a DAVIS346 camera such that it focuses through the BS and forms an imaging path. Test objects are displayed on a Kindle Paperwhite^{tm}, which does not employ a screen refresh rate and thus has no irradiance fluctuations detected by the EBS. At the other input of the BS is the imaged view of a white poster board which is illuminated by multiple fluorescent lights to enact a uniform screen of light. The screen and the BS form the injection path in the system. The BS, camera, and Kindle screen are pre-aligning such that no "ghost" images are formed. To maintain a properly enclosed system, the DAVIS346 is translated on a Thorlabs linear stage for generating events. A 16 mm lens maintains a horizontal FOV of 22° when used on the EBS camera. The camera is moved at a constant velocity of 2.5 mm/s, which is restricted by the lens FOV and size of BS (1" cube). This velocity v_p translates to 16.7 EBS pixels per second (0.06 seconds per pixel) as the object is moved and is restricted by the lens FOV and size of the BS.

Neutral density filters are placed at the BS inputs to individually modulate both path intensity levels and create combinations of object-to-padding levels. To explore how signal and noise event rate (and SNR) vary through optical biasing, an array of object and injection irradiance levels must be studied. The low-light region with high noise is sampled by targeting five object irradiances, each of which will receive four varying injection irradiances to reach an irradiance total (object + injection) in the stable regime. The targeted object irradiances and total irradiances are depicted in red and orange respectively in Figure 12 below.

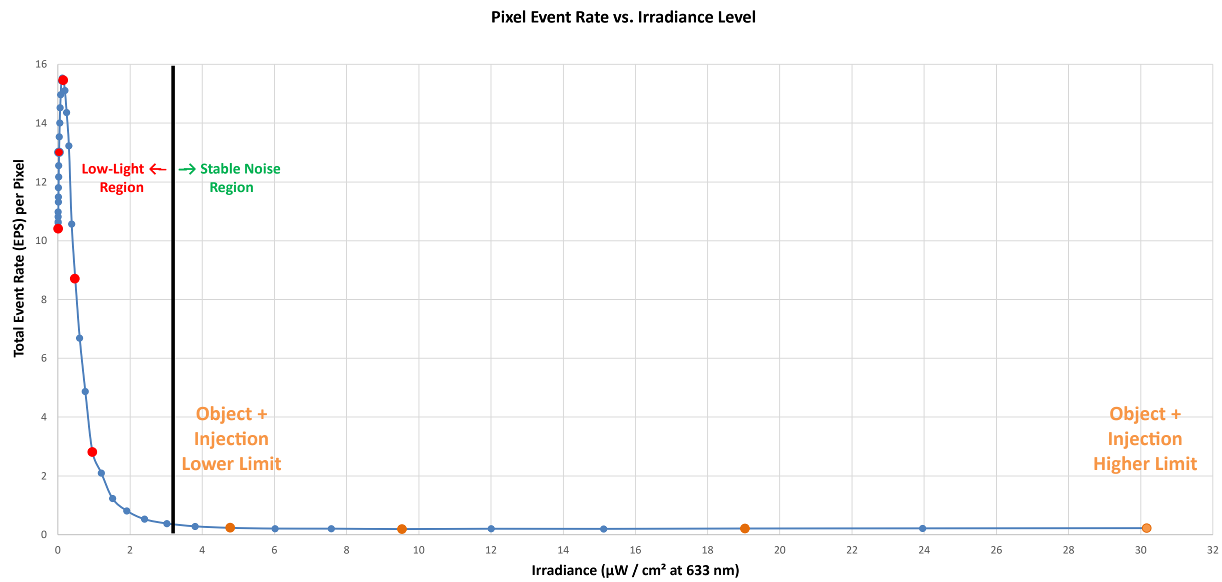

Figure 12. Marked object and total irradiances that are targeted for creating array of object and injection irradiance pairings.

To ensure that input light levels for both paths are well-known and to mitigate stray light in the system from entering the imaging or injection paths, the constructed optical system is placed in a low-reflectance enclosure with blackout fabric and a covering canopy. An opening in the enclosure allows for the injection path imaging from the poster board to remain unaltered.

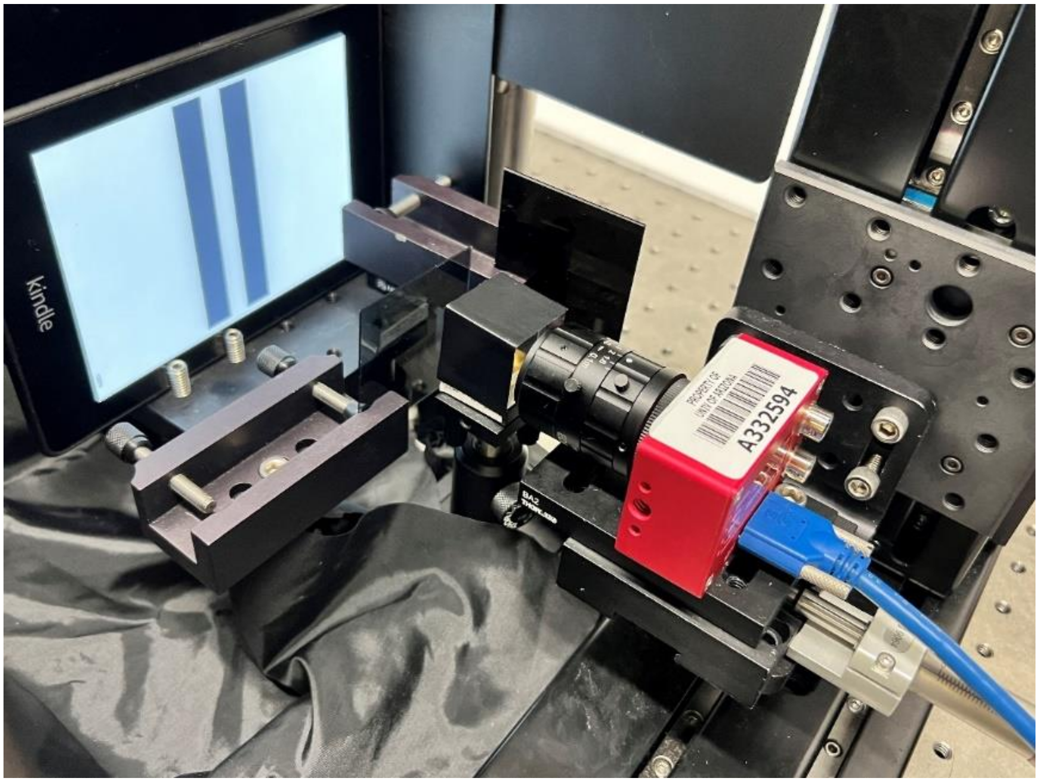

Figure 13. Optical biasing system with enclosure canopy removed.

A spatially symmetric test object consisting of black and white bars is loaded onto the kindle display and fixed directly inline of the imaging path. The black and white regions approximately cover 40 and 60% of the FOV respectively. Irradiance produced by both regions is individually measured at the input of the BS using a power meter by displaying full screen objects in black and white settings. Light intensity reaching the sensor will be some multiplicative factor from the transmission of the lens. Irradiances in the imaging arm for any ND filter attenuation setting are readily known from specified ND filter transmission percentages. Similarly, the input irradiance at the injection arm is also stepped down when a known ND filter is inserted. Table 3 below shows the per-pixel irradiance values targeted for each object (white region), injection, and sum irradiances across the 20 test cases.

Table 3. Total per-pixel irradiance (μW/cm^2 at 633 nm) for predicted object and injection setting pairs.

Object Irradiance Settings		**Injection Irradiance Settings**			
		Increasing Injection Level →			
		2.40	**12.01**	**19.03**	**30.16**
Decreasing Object Level ↓	**1.10**	3.50	13.11	20.13	31.26
	0.44	2.84	12.45	19.47	30.60
	0.11	2.51	12.12	19.14	30.27
	0.03	2.43	12.04	19.06	30.19
	0.004	2.40	12.01	19.03	30.16

Injecting light onto the sensor plane works to refine the resultant event stream of shot-noise events, as with BAFs and other denoising approaches. Optical biasing may be combined with other methods to further alleviate noise levels. The combined effect of optical biasing with a background activity filter for the best performing injection setting is studied to probe into the combined effect of both on SNR and overall event rates. The OrderNBackgroundActivityFilter is a readily available filter in jAER with minimal memory utilization for processing high noise streams [43]. The maximum integration time of a single pixel is ~$1/v_p$ (60 ms) for the object stimulus, indicating the approximate firing rate for pixels should not be higher. dT for the OrderNBackgroundActivityFilter is nominally set to 60 milliseconds for surveying composite effects of biasing with an added software filter.

Table 4. Default bias current parameters set for optical biasing experiment.

Bias Symbol	**Control of Bias**	**Value**
I_{pr}	Photoreceptor/Bandwidth	759.8 pA
I_{sf}	Source Follower Buffer/Bandwidth	95.0 pA
I_d	Change Amplifier	48.6 nA
I_{on}	ON Threshold	389.0 nA θ_{ON} = 21.2% (0.193 e-folds)
I_{off}	OFF Threshold	6.1 nA θ_{OFF} = -18.1% (-0.200 e-folds)
I_{refr}	Refractory Period	6.1 nA

Chapter 4: Experimental Results

In this Chapter, the full processed results for HPF and optical biasing experiments are presented. Data collection methods are also discussed.

4.1 Optical High-Pass Spatial Filtering

Here we present a collection of images corresponding to the recorded EBS output data and/or frame-based image data for the objects of interest for the implemented transmissive system. Data collection methods and analysis in terms of observed vs. predicted (theoretical) events or contrast enhancement with the HPF method are discussed.

Data was collected by individually placing each of the four total transition boundaries within the imaged view of the EBS. The EBS is then moved in a controlled manner to measure event output with and without the HPF enabled to determine low-contrast detection in terms of measured event rates. The performance is also qualified with the below images, captured when the transparency object is imaged at the center of the focal plane. The EBS motion is induced so that the irradiance corresponding to the higher transmittance region generates events when it is the "previous state" in Equation 8. Therefore, a step decrease in irradiance across EBS pixels is registered when imaging the unfiltered object. When the HPF is enabled, however, events will be registered as increases in irradiance (ON events) since the boundary edge is brighter than the background (as in Figure 8(c)).

As a means of evaluating the effectiveness of this EBS HPF method, the isolated (line-associated) region event rate (E_B) produced by each boundary edge in the non-HPF cases is compared to corresponding HPF-enabled EBS event rate ($E_E = A \cdot E_B$). Here, A denotes the HPF-generated contrast amplification, and the quantitative metric used to establish the validity of this method. The associated event rates per pixel are extracted via jAER with the CellStatsProber (CSP) information filter and a hot pixel filter enabled to suppress pixels that continuously misfire events when visual input is idle. Figures 14 – 17 qualitatively show the sets of frame-based and EBS views of each boundary with and without filtering.

The images show how each region and boundary exhibits non-uniformities and presents visible artifacts. These artifacts are products of the lithography process used to create the prototype photoresist slide. The required propagation of a coherent point source of light with a spatial/pinhole filter has the added complication of forming coherent diffraction patterns at the image plane. These patterns are detected by the EBS and create extraneous events, primarily when the HPF is disabled. Beneficially, however, these rings are unseen by the EBS after filtering as they are too low in contrast to detect. The detected diffraction rings are seen in the (c) quadrants of Figures 14-17. Therefore, steps for mitigating the event rates contributed by diffraction, and other artifacts, become necessary. As a result, Multiple samples of each boundary were taken and averaged when the boundaries did not span the entire image height or were surrounded by significant artifacts. Samples were smaller subsections of the boundaries, which were well-defined and least affected by clutter. These samples were taken to avoid measuring event rates that were not representative of contrasts predicted in Table 2. As the slide moves, the event rate was measured in the area (covered by subsection) immediately before and at each boundary. Thus, a baseline event rate formed by diffraction and artifacts is measured, which can then be subtracted from the measured event rate at each boundary such that HPF-induced events are distinguished. Examples of selective regions of interest (ROIs) are shown in Figure 18.

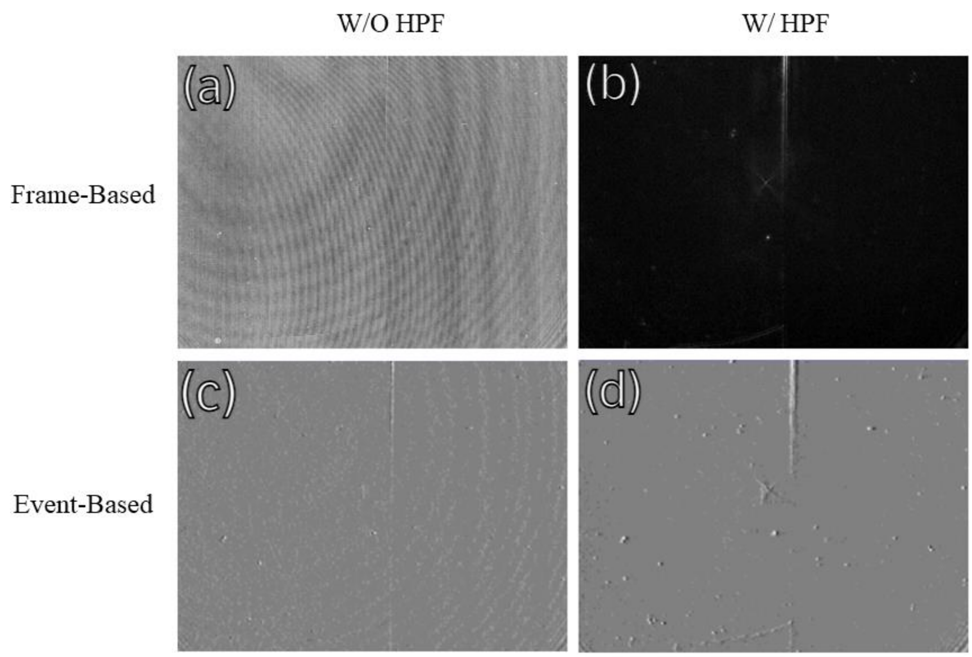

Figure 14. Standard (a) and EBS output (c) when HPF is disabled, and standard (b) and EBS output (d) when HPF is enabled for Boundary 1 between regions 1 and 2 (corresponding to an 8.17% average contrast).

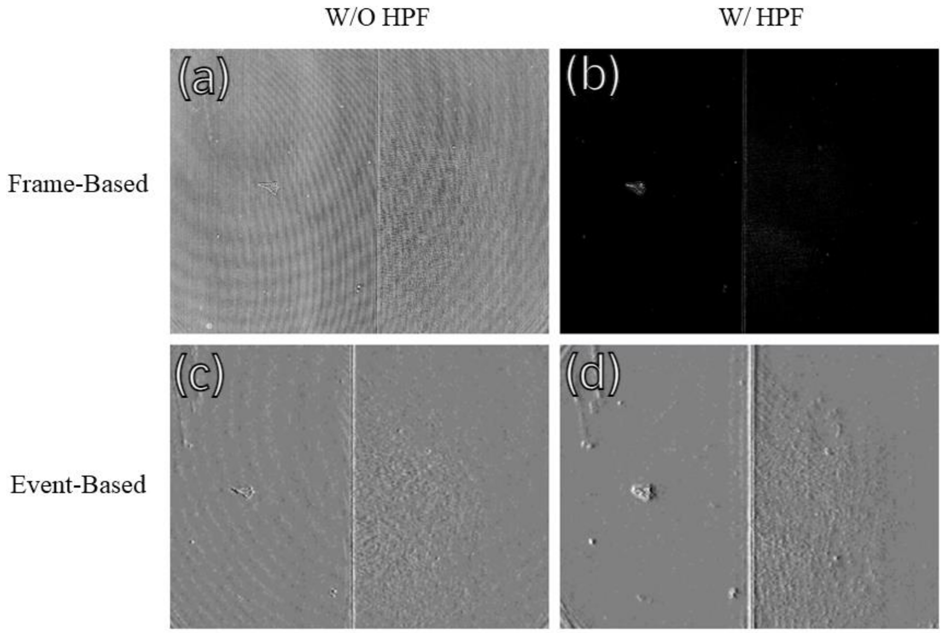

Figure 15. Standard (a) and EBS output (c) when HPF is disabled, and standard (b) and EBS output (d) when HPF is enabled for Boundary 2 between regions 2 and 3 (corresponding to an 6.69% average contrast).

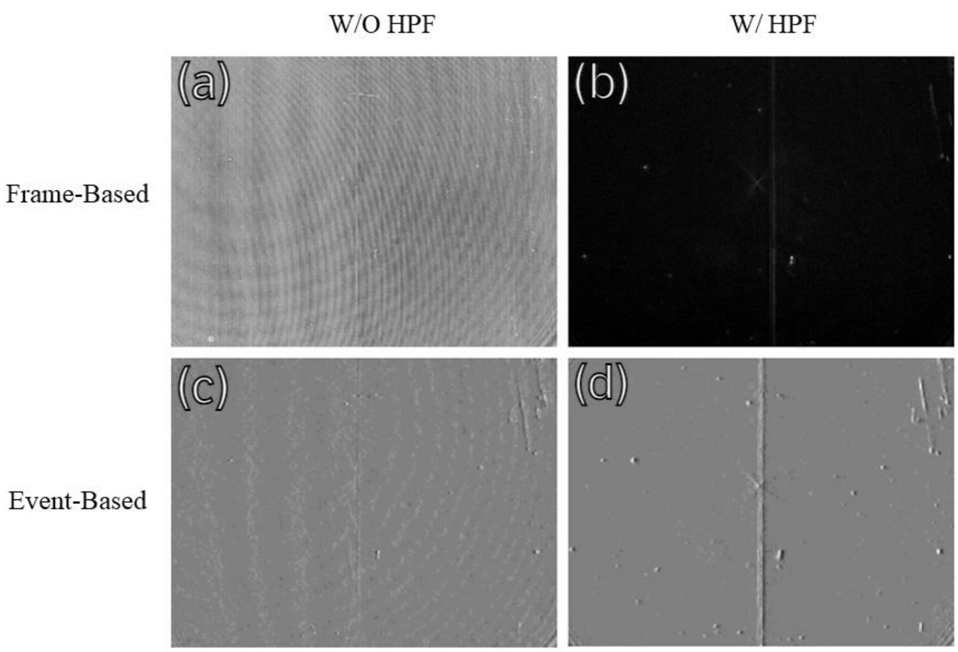

Figure 16. Standard (a) and EBS output (c) when HPF is disabled, and standard (b) and EBS output (d) when HPF is enabled for Boundary 3 between regions 3 and 4 (corresponding to an 5.41% average contrast).

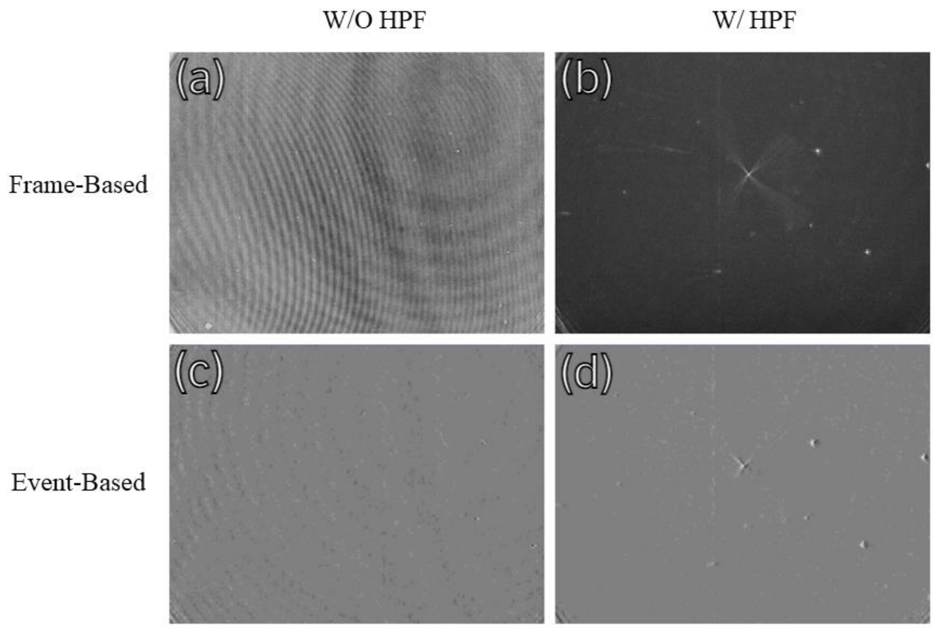

Figure 17. Standard (a) and EBS output (c) when HPF is disabled, and standard (b) and EBS output (d) when HPF is enabled for Boundary 4 between regions 4 and 5 (corresponding to an 3.53% average contrast).

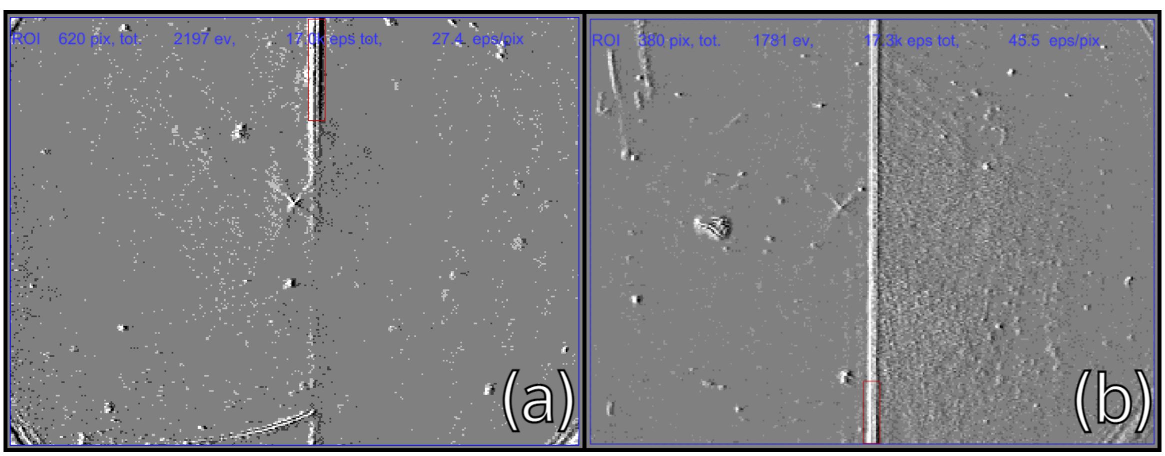

Figure 18. Example of selective ROI for case of broken/detached boundary (a). Example of selective ROI for case of high artifact/nonuniformity presence (b).

Presented here are the processed results for the transmissive HPF system:

Table 5. Experimental event rate productions at low-contrast boundaries (per 20 millisecond window).

	Boundary	1st	2nd	3rd	4th
Theoretical	**Non-HPF (Events per Second / Pixel)**	2.15 ± 0.05	1.90 ± 0.05	1.68 ± 0.04	1.33 ± 0.04
	HPF (Events per Second / Pixel)	34.72 ± 1.21	24.74 ± 0.98	17.81 ± 0.86	7.30 ± 0.45
	Contrast Amplification Factor (A)	16.1 ± 0.7	13.0 ± 0.6	10.6 ± 0.6	5.5 ± 0.4
Experimental	**Non-HPF (Events per Second / Pixel)**	1.83 ± 0.87	1.63 ± 1.18	1.07 ± 0.64	0.40 ± 0.71
	HPF (Events per Second / Pixel)	25.53 ± 0.65	19.10 ± 1.53	9.77 ± 1.06	1.27 ± 0.59
	Contrast Amplification Factor (A)	14.0 ± 6.7	11.7 ± 8.5	9.2 ± 5.6	3.2 ± 5.8

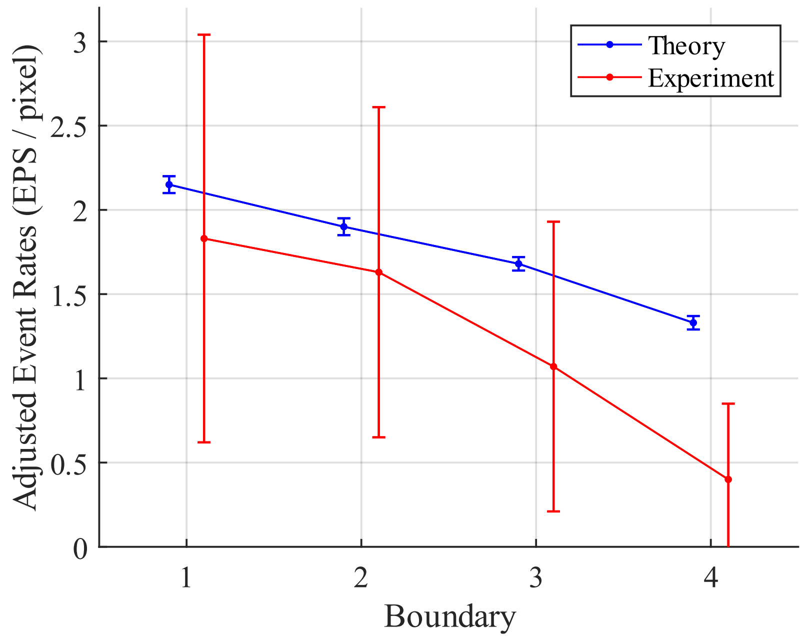

Figure 19. Adjusted theoretical and experimental event rates for non-HPF cases. NOTE: Small x-axes shifts added for improved visibility.

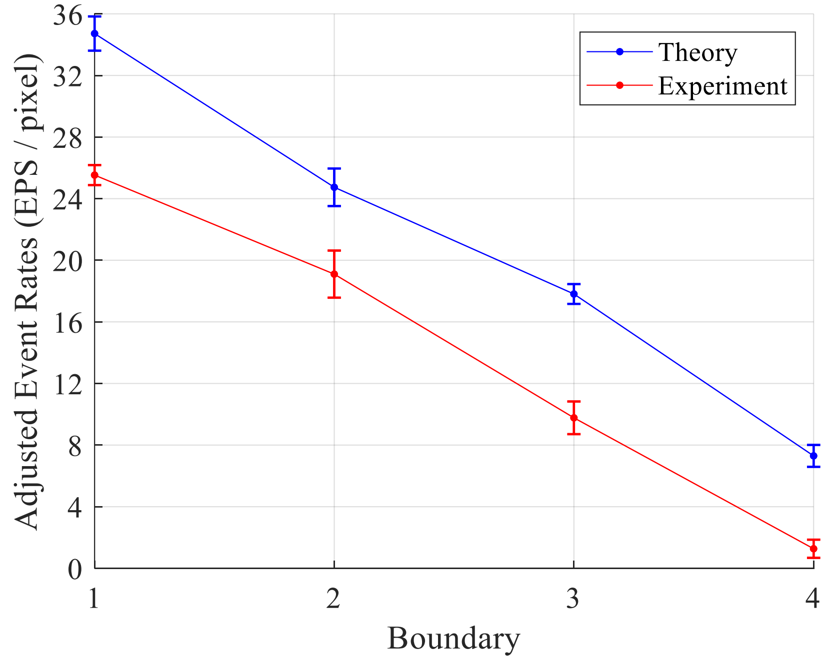

Figure 20. Adjusted theoretical and experimental event rates for HPF cases.

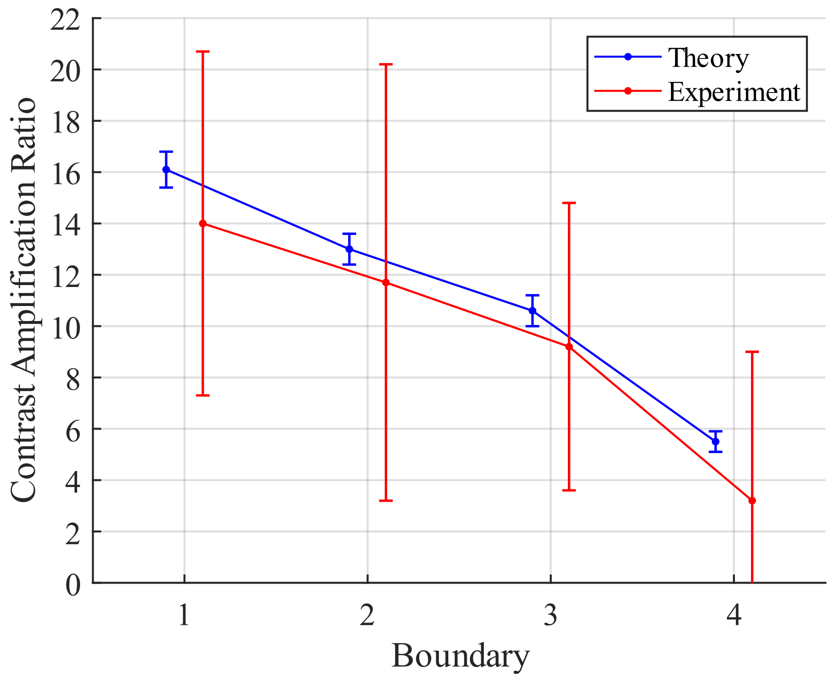

Figure 21. Theoretical and experimental contrast amplification ratios with error bars. NOTE: Small x-axes shifts added for improved visibility.

According to experimental results in Table 3 above, it is evident that an increase in event production occurs after HPF. Across the four low-contrast regions, High-Pass Filtering provides, on average, an amplification factor of 3.2 for the lowest contrast (Boundary 4). HPF boosts an imperceptible 3.53% average contrast edge to visible levels for the EBS. While there is a mismatch between theoretical and experimental results, discrepancies may be understood with the non-idealities in our optical implementation. Mainly, the custom photoresist slide has non-uniformities in the regions seen by our HPF system. When in place, the High-Pass Filter enhances the edges of all scene elements, such that both non-uniformities and desired region boundaries are amplified. Therefore, artifacts on optical components (i.e., dust, scratches, smears), vignetted elements, or an imperfectly blocked zero-frequency spot will be visible in HPF-view and generate unnecessary events, which degrade HPF signal-to-noise ratio. In Figures 14 to 17, artifacts are seen in the standard EBS view, and are amplified with the HPF. The quality of the prototype object used sets limits on low-contrast levels and event rates measured and will likely be demonstrated with further HPF development beyond proof-of-concept.

Diffraction artifacts may be mitigated (i.e., shorter wavelengths or partial coherence system) but are, to an extent, unavoidable with any coherence setup. The visibility of these patterns is decreased after HPF in our configuration but may still have a presence at higher source illumination levels or with a filter mask with lower cutoff frequencies. The size and optical quality of the mask will greatly improve the value of HPF when matched with scene spatial frequency combinations, and optimization is a goal for future work. As discussed in Chapter 2.3, having minimal background irradiance levels will maximize relative irradiance changes and detected objected contrasts. However, given the higher EBS noise limitation at low illumination levels (Figure 10), a careful balance between HPF event generation and noise level mitigation becomes an implicit consideration. Overall, the experiment results demonstrate a significant advantage of using Fourier-based optical filtering for low-contrast scenarios.

4.2 Optical Biasing

This section elaborates on data collection methods for optical biasing implementations discussed in section 3.4. Shown are a collection of images corresponding to the recorded EBS output data and standard image data for the object of interest in the optical biasing system. Similarly, images of event output with optical padding, and optical padding in combination with a noise background activity filter are exhibited in comparison to baseline profiles.

APS/EBS data is captured for static and in-motion cases in each of the five object settings without any artificial injection (by completely closing off injection window seen in Figure 13, as well as adding a high optical density (OD) ND filter in injection path). Similarly, the test object kindle is turned off when capturing APS frames, EBS outputs, and absolute irradiance levels from the standalone injection settings. For each of 20 test cases (five object settings, four injection settings), the appropriate neutral density filter pairs are set for the imaging and padding arms of the beam splitter setup. With each individual setting, an optical power meter (calibrated at 633 nm wavelength) is placed at the BS inputs to measure irradiances. Movement for generating events is induced by translating the EBS on a linear translation stage at set velocity. The EBS was configured with all nominal device parameters in jAER for this experiment, shown in Table 4.

Depictions of frame-based and EBS feeds for each baseline case before and after 10 μW$/cm^2$ at 633 nm (injection setting #2) is applied are seen Figures 22 – 25. An example of combining optical biasing with the enabled OrderNBackgroundActivityFilter is seen in Figure 26. Noise and signal event rates are measured for all event streams using the CSP information filter in jAER, and with a hot pixel filter enabled. With the CSP filter, multiple samples of bright bar region, dark bar region, and entire FOV are taken such that sectioned and total event rates of the imaged object are known. A normalized signal minus noise ratio ($R_{S\cdot N}$) is used as a metric to justly compare lowered signal event rates R_S and noise event rates R_N [17].

$$\boldsymbol{R_{S\cdot N} = \frac{R_S - R_N}{R_S + R_N}} \quad \textbf{(15)}$$

Where R_S consists of the total (ON + OFF) event rate when object is in motion, and R_N is the Static event rate for background (black) region. The EBS does not operate in the steady noise region discussed in Section 3.1. As a result, the measured signal event rates generated between the object's trailing and leading edges will inevitably contain a residual event rate of overlayed noise that cannot be completely filtered out.

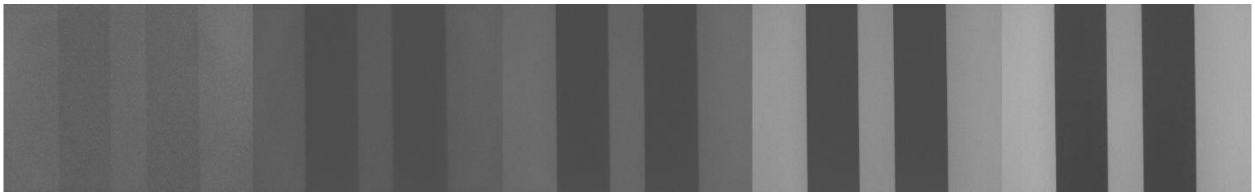

Figure 22. Standard APS frame output for five baseline kindle object settings in order of increasing object irradiance

Figure 23. Standard APS frame output for five baseline kindle object settings with injection setting #2 (~10 μW/cm^2 at 633 nm)

Figures 24-25 are examples of event-based views of the five baseline kindle object settings before and after biasing with injection setting #2 while the sensor is moved at constant velocity v_p.

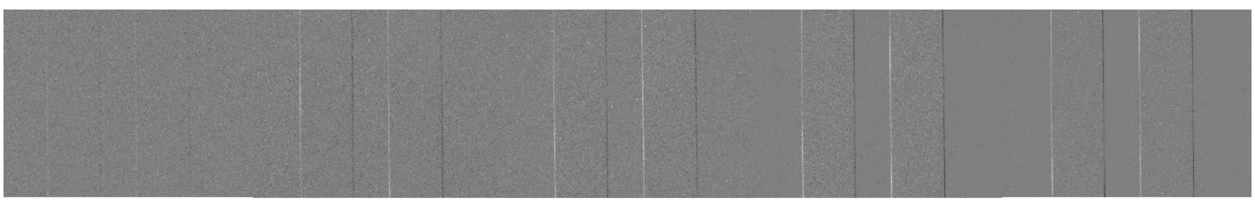

Figure 24. EBS frame output for five baseline kindle object settings in order of increasing irradiance

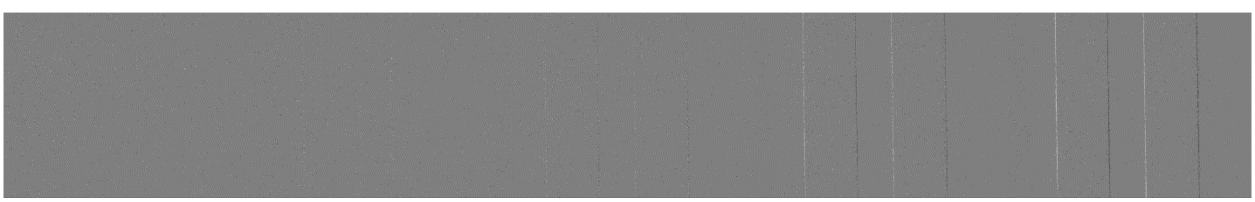

Figure 25. EBS output for five baseline kindle object settings with injection setting #2 (~10 μW/cm^2 at 633 nm)

Figure 26 compares EBS outputs before and after adding in BAF to the single best performing case (object setting #5 and injection setting #2). The BAF added is an OrderNBackgroundActivityFilter set with dT of 60 milliseconds. It is visually noted that although noise reduction is significant, so is event production for object edges.

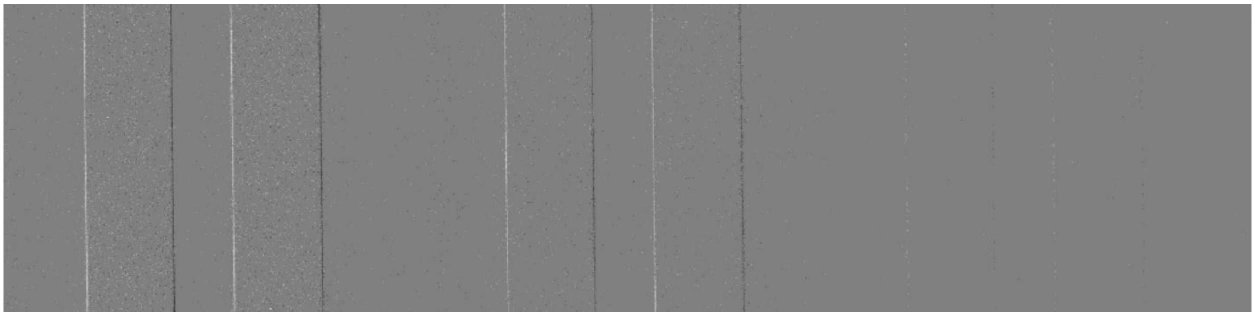

Figure 26. EBS Outputs for baseline object setting #5 (~2.68 μW/cm^2 at 633 nm) [Left], with injection setting #2 (~10 μW/cm^2 at 633 nm) [Middle], and injection setting #2 with OrderNBackgroundActivityFilter [Right]

Figure 27 shows the actual measured event rates compared with expected rates from Table 3 and depicts the distribution of the 20 different object-to-injection ratio test cases. Tables 6-10 hold the quantitative results of measured irradiance levels, Noise ER, Signal ER, and $R_{S \cdot N}$ for all optical biasing cases.

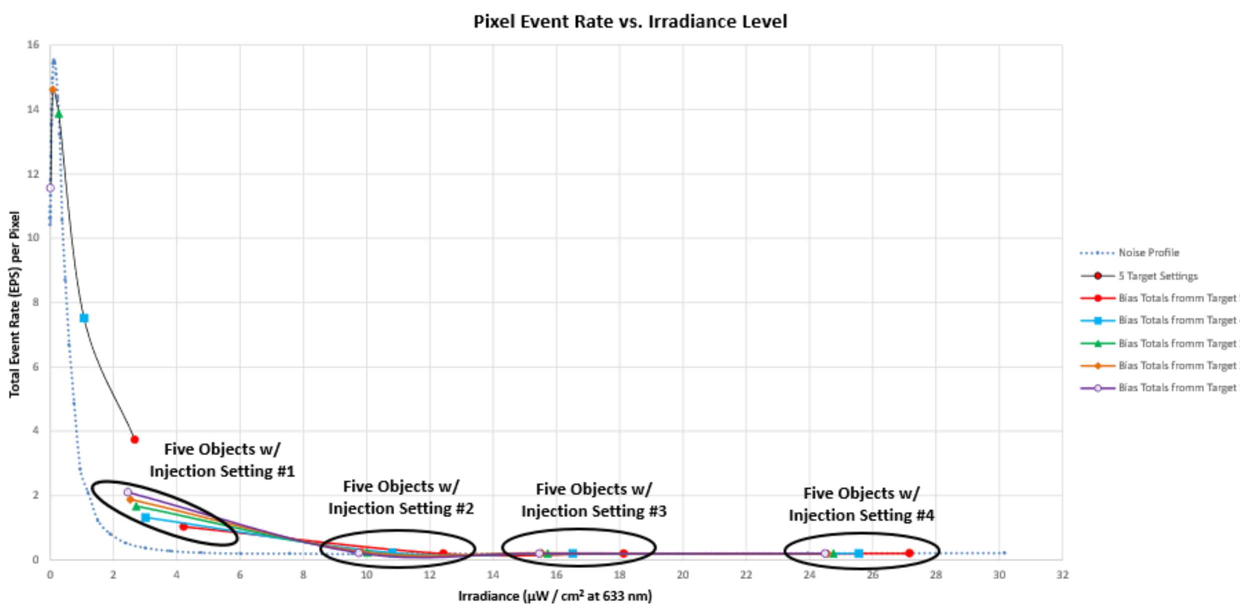

Figure 27. Measured object and biasing totals overlayed onto ambient illumination noise profile. Four Clusters of object + injection irradiances circled.

Table 6. Irradiance totals (uW/cm^2 at 633 nm) and injection-to-object irradiance ratios for object and injection setting pairs.

Object Irradiance Settings			Injection Irradiance Settings			
			Increasing Injection Level →			
			#1	#2	#3	#4
			2.45	**9.75**	**15.45**	**24.49**
Decreasing Object Level ↓	#1	**2.68**	5.13 0.9	12.43 3.6	18.13 5.8	27.17 9.1
	#2	**1.07**	3.52 2.3	10.82 9.1	16.52 14.4	25.56 22.9
	#3	**0.27**	2.72 9.1	10.02 36.1	15.72 57.2	24.76 90.7
	#4	**0.08**	2.53 30.6	9.83 121.9	15.54 193.1	24.57 306.1
	#5	**0.01**	2.46 245	9.76 975	15.46 1545	24.50 2449

Note: First entry is irradiance total, and second entry is injection-to-object irradiance ratio

Table 7. Noise event rates [Events / second per pixel] for object/injection pairs.

Object Setting	Average ER Without Injection (Baseline)	Injection Setting							
		1	Reduction Factor	2	Reduction Factor	3	Reduction Factor	4	Reduction Factor
5	**8.4**	2.1	4.0	0.204	41.2	0.206	40.8	0.211	39.8
4	**15.7**	2.3	6.8	0.232	67.7	0.208	75.5	0.206	76.2
3	**15.5**	2.2	7.0	0.255	60.8	0.214	72.4	0.216	71.8
2	**16.3**	2.0	8.2	0.276	59.1	0.223	73.1	0.206	79.1
1	**12.3**	2.1	5.9	0.215	57.2	0.199	61.8	0.196	62.8

Table 8. Signal event rates [Events / second per pixel] for object/injection pairs.

Object Setting	Average ER Without Injection (Baseline)	Injection Setting							
		1	Reduction Factor	2	Reduction Factor	3	Reduction Factor	4	Reduction Factor
5	**16.6**	7.95	2.1	2.35	7.1	1.70	9.8	1.09	15.3
4	**20.8**	5.90	3.5	1.30	16.0	0.75	27.6	0.52	39.9
3	**20.9**	3.75	5.6	0.53	39.8	0.33	63.0	0.28	75.2
2	**19.2**	2.65	7.2	0.37	52.4	0.27	71.2	0.23	82.9
1	**12.7**	2.35	5.4	0.25	51.8	0.21	60.5	0.18	72.6

Table 9. $R_{S\cdot N}$ values for object/injection pairs

Object Setting	$R_{S\cdot N}$ Value Without Injection (Baseline)	Injection Setting							
		1	Improvement Factor	2	Improvement Factor	3	Improvement Factor	4	Improvement Factor
5	**0.33**	0.58	1.8	0.84	2.5	0.78	2.4	0.68	2.1
4	**0.14**	0.44	3.1	0.70	5.0	0.57	4.0	0.43	3.1
3	**0.15**	0.26	1.7	0.35	2.3	0.22	1.5	0.13	0.9
2	**0.08**	0.14	1.8	0.14	1.8	0.08	1.0	0.06	0.8
1	**0.02**	0.06	3.0	0.07	3.5	0.02	1.0	0.01	0.5

Table 10. Noise ER, Signal ER, and $R_{S\cdot N}$ values for optical biasing paired with OrderNBackgroundActivityFilter for best injection case (injection setting #2 / ~10 μW/cm^2 at 633 nm) for each object setting. Note: ER number precision measured is dictated by jAER CSP filter

Object Setting	Noise ER [Events / sec per pixel]	Signal ER [Events / sec per pixel]	$R_{S\cdot N}$ Value	Baseline $R_{S\cdot N}$ Value	Improvement Factor
5	0.0076	0.510	**0.97**	**0.33**	**2.9**
4	0.0052	0.120	**0.92**	**0.14**	**6.6**
3	0.0101	0.046	**0.64**	**0.15**	**4.3**
2	0.0044	0.012	**0.4**	**0.08**	**5.0**
1	0.0057	0.0061	**0.03**	**0.02**	**1.5**

Chapter 5: Conclusions

Discussed here are key findings, takeaways, suggested improvements, and work moving forward for the two proposed methods discussed in this thesis.

5.1 Optical Spatial High-Pass Filtering

This work reveals the effectiveness of optical spatial high-pass filtering for improving Event-Based Sensors' low-contrast detection. As opposed to modifying pixel circuitry to alter contrast threshold characteristics, the EBS images low-contrast transparency objects with a 4f HPF imaging system. We demonstrate how this experimental method compares with contrast amplification theoretical predictions. The HPF system is capable of magnifying and detecting contrasts as low as 3.53% and may provide greater results when system optimizations are considered. EBS detection performance in low-contrast scenarios is heightened through a spatial filtering system which filters through the information vital to the change-detection chain at the speed of light.

Drawbacks of the HPF method (active coherent illumination, diffraction, background irradiance, Fourier mask size, etc.) and potential mitigation techniques are discussed for improvement suggestions. Integration with HPF enables a higher SNR with EBS, helping to mitigate an important limitation in EBS adoption. The broad utility of EBS cameras allows high spatial filtering to offer benefits in many fields. Tracking transparent specimens as in phase contrast microscopy, high-speed matched filtering, and many astronomy applications which image spatially coherent stars, are few implementations for EBS-HPF systems. Broadly, this method supplements EBS viability to a host of existing applications involving coherent imaging.

Future work may entail implementations of configurable HPF systems with scene-specific optimizations for absolute irradiance levels, mask size/shape, diffractions, and the 4f configuration. Such designs may also be readily integrated with existing EBS feedback-controlled systems[18] with the potential of multiplicative performance gain. A properly configured reflective HPF system is a more suitable implementation for detection and tracking of real-world objects, with great potential to be condensed as an add-on lens to EBS cameras. This is opposed to usage-constrained transparencies which are in the direct line of the optical path, as in this experiment. This work may also guide future developments of optical hardware enhancements to improve neuromorphic imaging systems as opposed to doing strictly in electronics and software.

5.2 Optical Biasing

Optical biasing can introduce up to 5x boost in normalized signal minus noise ratio, prior to post-imaging noise filtering. The $R_{S \cdot N}$ values by superimposing a BAF with optical biasing are greatly improved, which suggests that the multiplicative effect of combining this method with other noise reduction methods may be significant. However, the absolute level of signal event rates is quite low in these cases, which may result in poor feature extraction of the object of interest. The main cost with this method is a reduction in overall object contrast, which notably limits signal event rate. Event-generation in this set configuration may be boosted by increasing overall object contrast with respect to background, or by increasing the effective object velocity of the object on the focal plane as it traverses the FOV. This method may potentially be implemented as an EBS camera accessory in the form of a modified optoelectronic lens and scaled up further with a supplementary padding-current source in the EBS pixel circuit, as opposed to noise-correction approaches predominantly done with software. EBS performance with optical biasing was studied under varied illumination levels, however, full characterization across varying object sizes, velocities, object-to-background ratios, and key sensor parameters was not included. These variables along with tuning bias parameters are expected to alter performance significantly, is a higher dimensional and future suggested study. Mapping low-noise tradeoffs with this method and others to idealize the sensor's capacity is apt, especially as demand for EBS cameras in the more noise-sensitive infrared region progresses. Low light conditions are often encountered in astronomy, microscopy, or noninvasive imaging, which are only a few reasons to motivate improved EBS behavior under such conditions. This work may guide these novel sensors' future development and suggest improved practices of photocurrent biasing moving forward.

Appendix

Although the emphasis of the HPF study utilized a transmissive system to indicate the value of contrast amplification via an optical HPF, an abbreviated analysis was also performed on a reflective configuration. Figure 28 depicts a constructed system operating at a high power so that a strong reflected signal off an illuminated object may propagate through the 4f system. The feature of interest is a vertical grey bar against a white background. The image view of this bar was captured via the standard grayscale feed of the DAVIS346. A qualitative comparison between the image view of this object was done with and without the HPF in place.

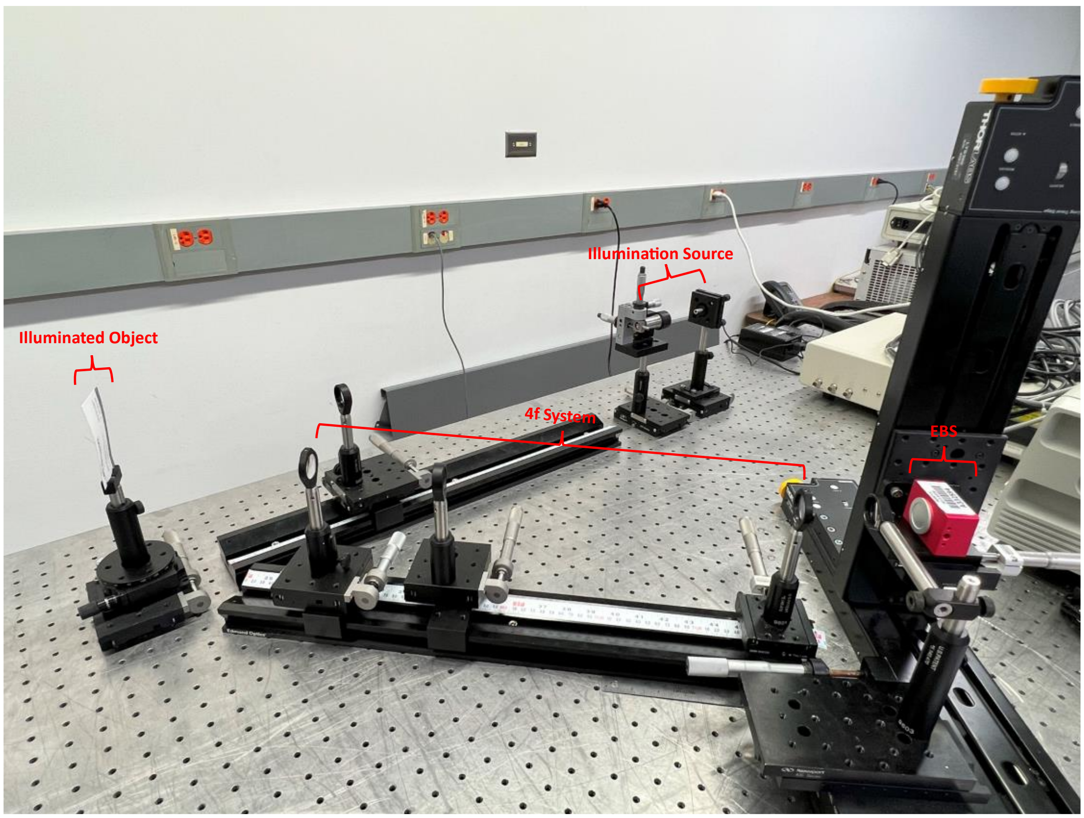

Figure 28. Overall Reflective HPF System layout with subsystems labelled.

The results from the reflective system HPF experiment are seen in Figure 29. Qualitatively, there is great similarity between the image reaching the sensor before and after placing the HPF mask in the optical path. Both images depict similar granular features from reflection of the illumination source off the rough object.

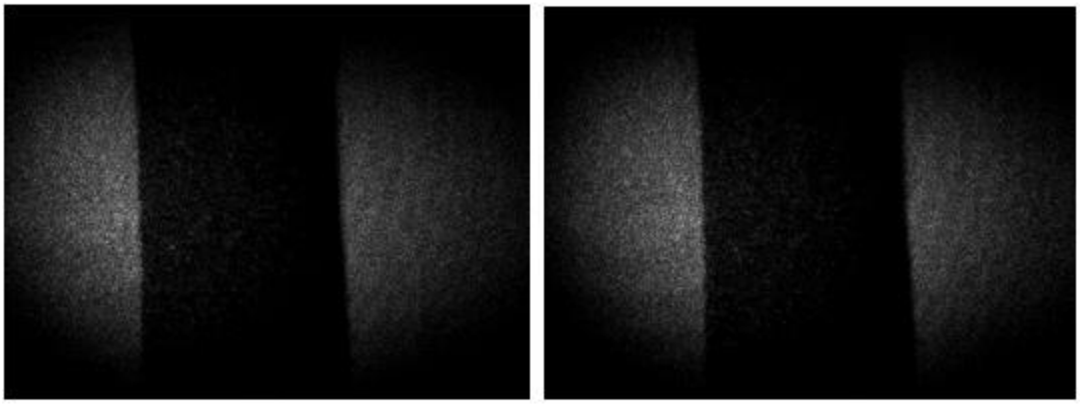

Figure 29. Object of interest without (Left) and with (Right) HPF in reflective system.

It is observed that Optical High-Pass Filtering does not produce noticeable changes (or amplification) in the optical field which reaches the sensor. A major caveat of using this reflective technique is the inconvenience that arises from using coherent light. Laser speckle is a biproduct of coherent illumination that occurs on a rough surface when light reflects or scatters from unequal parts of the illuminated surface to produce an observable granular pattern. Speckle is a high frequency signal that overlays the illuminated object of interest, thus degrading the effectiveness of a high-pass filter. Edge detection becomes dependent on the resolution of speckle, strength of illumination source, surface properties and reflectivity, as well as distance and size of object. Low-resolution speckle paired with the HPF method could perhaps be useful for edge detection but was not explored in this study. High-resolution speckle (as seen in Figure 29) may shroud the EBS output with events through these rapid irradiance fluctuations. Determining the speckle content of a scene, how to mitigate speckle, and determine when edge-detection can still be used for the purposes of EBS detection and tracking are suggested future developments from this paper.

References

[1] Lichtsteiner, Patrick, Christoph Posch, and Tobi Delbruck, “A 128 x 128 120 dB 15 μs Latency Asynchronous Temporal Contrast Vision Sensor,” IEEE journal of solid-state circuits, 43 (2), 566 –576 (2008). https://doi.org/10.1109/JSSC.2007.914337 Google Scholar

[2] Y. Nozaki and T. Delbruck, "Temperature and Parasitic Photocurrent Effects in Dynamic Vision Sensors," in *IEEE Transactions on Electron Devices*, vol. 64, no. 8, pp. 3239-3245, Aug. 2017, doi: 10.1109/TED.2017.2717848.

[3] Peter N. McMahon-Crabtree, Wellesley Pereira, Robert Crow, Richard Preston, Lucas Kulesza, Ryan Crowell, Christian P. Morath, Diana Maestas, Zachry Theis, Patricia Sablan, "Automated characterization techniques and testbeds for event-based cameras," Proc. SPIE 12233, Infrared Remote Sensing and Instrumentation XXX, 122330B (30 September 2022); https://doi.org/10.1117/12.2634166

[4] A. Amir et al., "A Low Power, Fully Event-Based Gesture Recognition System," 2017 IEEE Conference on Computer Vision and Pattern Recognition (CVPR), 2017, pp. 7388-7397, doi: 10.1109/CVPR.2017.781.

[5] M. Litzenberger, A. N. Belbachir, N. Donath, G. Gritsch, H. Garn, B. Kohn, C. Posch, and S. Schraml, “Estimation of vehicle speed based on asynchronous data from a silicon retina optical sensor,” in IEEE Intell. Transp. Sys. Conf., 2006, pp. 653–658

[6] A. Glover and C. Bartolozzi, “Event-driven ball detection and gaze fixation in clutter,” in IEEE Int. Conf. Intell. Robot. Syst. (IROS), 2016

[7] Rebecq, Henri, “High speed and high dynamic range video with an event camera,” IEEE Transactions on Pattern Analysis and Machine Intelligence, (2019)

[8] Mueggler, Elias, Basil Huber, and Davide Scaramuzza, “Event-based, 6-DOF pose tracking for high-speed maneuvers,” in 2014 IEEE/RSJ International Conference on Intelligent Robots and Systems, (2014).

[9] H. Rebecs, R. Ranftl, V. Koltun and D. Scaramuzza, "Events-To-Video: Bringing Modern Computer Vision to Event Cameras," *2019 IEEE/CVF Conference on Computer Vision and Pattern Recognition (CVPR)*, 2019, pp. 3852-3861, doi: 10.1109/CVPR.2019.00398.

[10] Cox, Joseph, and Nicholas Morley, “Tracking from a moving platform with the Dynamic Vision Sensor,” Computational Imaging IV.International Society for Optics and Photonics, 10990 (2019). https://doi.org/10.1117/12.2518761 Google Scholar

[11] iniVation. (2020, May). *Understanding the performance of neuromorphic event-based ... - inivation*. Understanding the Performance of Neuromorphic Event-based Vision Sensors. Retrieved April 13, 2023, from https://inivation.com/wp-content/uploads/2020/05/White-Paper-May-2020.pdf.

[12] IniVation, “IniVation Devices Specification”, from https://inivation.com/wp-content/uploads/2021/08/2021-08-iniVation-devices-Specifications.pdf

[13] Pan, Liyuan, “Bringing a blurry frame alive at high frame-rate with an event camera,” in Proceedings of the IEEE Conference on Computer Vision and Pattern Recognition, (2019). https://doi.org/10.1109/CVPR41558.2019 Google Scholar

[14] Pini, Stefano, “Video synthesis from Intensity and Event Frames,” in International Conference on Image Analysis and Processing, (2019). https://doi.org/10.1007/978-3-030-30642-7 Google Scholar

[15] C. Posch, T. Serrano-Gotarredona, B. Linares-Barranco and T. Delbruck, "Retinomorphic Event-Based Vision Sensors: Bioinspired Cameras With Spiking Output," in *Proceedings of the IEEE*, vol. 102, no. 10, pp. 1470-1484, Oct. 2014, doi: 10.1109/JPROC.2014.2346153.

[16] Barth, F. G., Humphrey, J. A., & Srinivasan, M. V. (2012). *Frontiers in sensing: from biology to engineering* (pp. 86-98). Amsterdam: Springer.

[17] T. Delbruck, R. Graca and M. Paluch, "Feedback control of event cameras," in *2021 IEEE/CVF Conference on Computer Vision and Pattern Recognition Workshops (CVPRW)*, Nashville, TN, USA, 2021 pp. 1324-1332.

[18] G. Gallego, et al.,"Event-Based Vision: A Survey" in IEEE Transactions on Pattern Analysis & Machine Intelligence, vol. 44, no. 01, pp. 154-180, 2022.

[19] Brian J. McReynolds, Rui P. Graca, and Tobi Delbruck "Experimental methods to predict dynamic vision sensor event camera performance," Optical Engineering 61(7), 074103 (25 July 2022). https://doi.org/10.1117/1.OE.61.7.074103

[20] SensorsINI. *SensorsINI/Jaer: Java tools for address-event representation (AER) neuromorphic vision and audio sensor processing*. GitHub, from https://github.com/SensorsINI/jaer

[21] iniVation. *Get started · DV*. Retrieved April 24, 2023, from https://inivation.gitlab.io/dv/dv-docs/docs/getting-started/

[22] T. Serrano-Gotarredona and B. Linares-Barranco, “A 128 128 1.5% contrast sensitivity 0.9% FPN 3 ms latency 4 mW asynchronous frame-free dynamic vision sensor using transimpedance preamplifiers,” IEEE J. Solid-State Circuits, vol. 48, no. 3, pp. 827–838, Mar. 2013.

[23] Boettiger, James P., "A Comparative Evaluation of the Detection and Tracking Capability Between Novel Event Based and Conventional Frame-Based Sensors" (2020). Theses and Dissertations. 3154. https://scholar.afit.edu/etd/3154

[24] M. Yang, S. -C. Liu and T. Delbruck, "A Dynamic Vision Sensor With 1% Temporal Contrast Sensitivity and In-Pixel Asynchronous Delta Modulator for Event Encoding," in *IEEE Journal of Solid-State Circuits*, vol. 50, no. 9, pp. 2149-2160, Sept. 2015, doi: 10.1109/JSSC.2015.2425886.

[25] Moeys, Diederik Paul & Corradi, Federico & Li, Chenghan & Bamford, Simeon & Longinotti, Luca & Voigt, Fabian & Berry, Stewart & Taverni, Gemma & Helmchen, Fritjof & Delbruck, Tobi. (2017). A Sensitive Dynamic and Active Pixel Vision Sensor for Color or Neural Imaging Applications. IEEE Transactions on Biomedical Circuits and Systems. PP. 1-14. 10.1109/TBCAS.2017.2759783.

[26] S. Guo and T. Delbruck, "Low Cost and Latency Event Camera Background Activity Denoising," in *IEEE Transactions on Pattern Analysis and Machine Intelligence*, vol. 45, no. 1, pp. 785-795, 1 Jan. 2023, doi: 10.1109/TPAMI.2022.3152999.

[27] M. Litzenberger *et al*., "Vehicle Counting with an Embedded Traffic Data System using an Optical Transient Sensor," *2007 IEEE Intelligent Transportation Systems Conference*, 2007, pp. 36-40, doi: 10.1109/ITSC.2007.4357700.

[28] R. Berner, C. Brandli, and M. Zannoni, “Data rate control for event- ¨ based vision sensor,” U.S. pat. req. 20180189959:A1, Jul. 2018. [Online]. Available: https : / / patentimages . storage . googleapis . com / 69 / 8d / fe / afaa1ae1d2d0ef / US20180189959A1.pdf.

[29] Goodman, J. W. (1996). Coherent Optical Information Processing Systems. In *Introduction to Fourier Optics*. essay, McGraw-Hill.

[30] Yelleswarapu CS, Kothapalli SR, Rao DV. Optical Fourier techniques for medical image processing and phase contrast imaging. Opt Commun. 2008 Apr 1;281(7):1876-1888. doi: 10.1016/j.optcom.2007.05.072. PMID: 18458764; PMCID: PMC2367331.

[31] Graca, Rui and Tobi Delbrück. "Unraveling the paradox of intensity-dependent DVS pixel noise." ArXiv abs/2109.08640 (2021): n. pag.

[32] G. Chen, H. Cao, J. Conradt, H. Tang, F. Rohrbein and A. Knoll, "Event-Based Neuromorphic Vision for Autonomous Driving: A Paradigm Shift for Bio-Inspired Visual Sensing and Perception," in *IEEE Signal Processing Magazine*, vol. 37, no. 4, pp. 34-49, July 2020, doi: 10.1109/MSP.2020.2985815.

[33] Hamann, Friedhelm and Guillermo Gallego. "Stereo Co-capture System for Recording and Tracking Fish with Frame- and Event Cameras." *ArXiv* abs/2207.07332 (2022): https://doi.org/10.48550/arXiv.2207.07332

[34] K. Zhang, Y. Zhao, Z. Chu, et al. "Event-based vision in magneto-optic Kerr effect microscopy." *AIP Advances 12*, 095315 (2022); https://doi.org/10.1063/5.0090714

[35] Clément Cabriel, Christian Specht, and Ignacio Izeddin. "Event-based sensor for fast and dense single-molecule localization microscopy (Conference Presentation)", Proc. SPIE PC12386, Single Molecule Spectroscopy and Superresolution Imaging XVI, PC123860G (15 March 2023); https://doi.org/10.1117/12.2648971

[36] G.Cohen, S.Afshar, and A. van Schaik. "Approaches for Astrometry using Event-Based Sensors", The Advanced Maui Optical and Space Surveillance Technologies Conference (2018); https://ui.adsabs.harvard.edu/abs/2018amos.confE..38C/abstract

[37] Y. Hu, S.-C. Liu, and T. Delbruck, "v2e: From video frames to realistic DVS events," in Proceedings of the IEEE/CVF Conference on Computer Vision and Pattern Recognition, 2021, pp. 1312–1321. [Online]. Available: https : / / openaccess . thecvf . com / content / CVPR2021W / EventVision / html / Hu v2e From Video Frames to Realistic DVS Events CVPRW 2021 paper.html.

[38] T. Finateu, A. Niwa, D. Matolin, K. Tsuchimoto, A. Mascheroni, E. Reynaud, P. Mostafalu, F. Brady, L. Chotard, F. LeGoff, H. Takahashi, H. Wakabayashi, Y. Oike, and C. Posch, "5.10 a 1280x720 Back-Illuminated stacked temporal contrast Event-Based vision sensor with 4.86um pixels, 1.066GEPS readout, programmable Event-Rate controller and compressive Data-Formatting pipeline," in 2020 IEEE International Solid- State Circuits Conference - (ISSCC), Feb. 2020, pp. 112–114. DOI: 10.1109/ISSCC19947.2020.9063149.

[39] R. Graca, B. McReynolds, and T. Delbruck, "Shining light on the DVS pixel: A tutorial and discussion about biasing and optimization," in Proceedings of the IEEE/CVF Conference on Computer Vision and Pattern Recognition (CVPR) Workshops, Jun. 2023.

[40] R. Graca, B. McReynolds, and T. Delbruck, "Optimal biasing and physical limits of DVS event noise," in 2023 International Image Sensor Workshop (IISW), May 2023. DOI: 10 . 48550 / arXiv. 230404019.

[41] B. McReynolds, R. Graca, and T. Delbruck, Exploiting alternating DVS shot noise event pair statistics to reduce background activity rates, 2023.

[42] Tobi Delbruck. Frame-free dynamic digital vision. In Proceedings of Intl. Symp. on Secure-Life Electronics, Advanced Electronics for Quality Life and Society, volume 1, pages 21– 26. Citeseer, 2008

[43] A Khodamoradi and R Kastner, “O(N)-Space spatiotemporal filter for reducing noise in neuromorphic vision sensors,” IEEE Transactions on Emerging Topics in Computing, vol. PP, no. 99, pp. 1–1, 2017, ISSN: 2168-6750. DOI: 10 . 1109 / TETC . 2017 . 2788865. [Online]. Available: http://dx.doi.org/10.1109/TETC.2017.2788865.

[44] Kowalczyk, Marcin, and Tomasz Kryjak. "Hardware architecture for high throughput event visual data filtering with matrix of IIR filters algorithm." *2022 25th Euromicro Conference on Digital System Design (DSD)*. IEEE, 2022.

[45] Barrios-Avilés, J.; Rosado-Muñoz, A.; Medus, L.D.; Bataller-Mompeán, M.; Guerrero-Martínez, J.F. Less Data Same Information for Event-Based Sensors: A Bioinspired Filtering and Data Reduction Algorithm. *Sensors* **2018**, *18*, 4122. https://doi.org/10.3390/s18124122

[46] Rios-Navarro, A., Guo, S., Abarajithan, G., Vijayakumar, K., Linares-Barranco, A., Aarrestad, T., ... & Delbruck, T. (2023). Within-Camera Multilayer Perceptron DVS Denoising. *arXiv preprint arXiv:2304.07543*

[47] C. Li, L. Longinotti, F. Corradi, and T. Delbruck, “A 132 by 104 10um-Pixel 250uW 1kefps dynamic vision sensor with Pixel-Parallel noise and spatial redundancy suppression,” in 2019 Symposium on VLSI Circuits, Jun. 2019, pp. C216–C217. DOI: 10.23919/VLSIC.2019.8778050.

[48] IniVation, “IniVation Developer Frequently Asked Questions”, from https://inivation.com/developer/faq/

[49] DARPA Announces Research Teams to Develop Intelligent Event-Based Imagers. DARPA RSS. (n.d.). (July 2, 2021), from https://www.darpa.mil/news-events/2021-07-02

[50] Claudio Jakobson, Rami Fraenkel, Nimrod Ben Ari, Roman Dobromislin, Niv Shiloah, Tomer Argov, Willie Freiman, Gal Zohar, Lidia Langof, Oren Ofer, Rahel Elishkov, Edan Shunem, Michael Labilov, Menashe Alcheck, Yiftah Kalfa, Michal Nitzani, Yoram Karni, Itay Shtrichman, and Tuvy Markovitz "Event-based SWIR sensor", Proc. SPIE 12107, Infrared Technology and Applications XLVIII, 1210704 (27 May 2022); https://doi.org/10.1117/12.2618290

[51] DARPA. (n.d.). *Defense Advanced Research Projects Agency (DARPA) Defense-Wide Justification Book* . Volume 1-143. Retrieved April 14, 2023, from https://www.darpa.mil/attachments/U_RDTE_MJB_DARPA_PB_2023_APR_2022_FINAL.pdf